










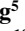






RESEARCH ARTICLE

10.1029/2022MS003397

Uncertainty and Emergent Constraints on Enhanced Ecosystem Carbon Stock by Land Greening

Key Points:

- A globally enhanced ecosystem C stock (ECS) by land greening has been detected since the 1980s from 40 global models
- The sensitivity of gross primary productivity to leaf area index (LAI) is the largest contributor to the modeled greening effect on ECS uncertainty
- This study estimated the effect of global greening on ECS with the emergent constraint method

Chenyu Bian^{1,2} , Jianyang Xia^{1,2} , Xuanze Zhang³ , Kun Huang^{1,2} , Erqian Cui^{1,2} , Jian Zhou^{1,2,4} , Ning Wei^{1,2} , Ying-Ping Wang⁵ , Danica Lombardozzi⁶ , Daniel S. Goll⁷ , Jürgen Knauer⁸ , Vivek Arora⁹, Wenping Yuan¹⁰, Stephen Sitch¹¹ , Pierre Friedlingstein¹² , and Yiqi Luo⁴ 

¹Zhejiang Tiantong Forest Ecosystem National Observation and Research Station, Institute of Eco-Chongming, School of Ecological and Environmental Sciences, East China Normal University, Shanghai, China, ²Research Center for Global Change and Complex Ecosystems, East China Normal University, Shanghai, China, ³Key Laboratory of Water Cycle and Related Land Surface Processes, Institute of Geographical Sciences and Natural Resources Research, Chinese Academy of Sciences, Beijing, China, ⁴School of Integrative Plant Science, Cornell University, Ithaca, NY, USA, ⁵CSIRO Oceans and Atmosphere, Aspendale, VIC, Australia, ⁶Terrestrial Sciences Section, Climate and Global Dynamics, National Center for Atmospheric Research, Boulder, CO, USA, ⁷LSCE/IPSL, CEA-CNRS-UVSQ, Université Paris Saclay, Gif sur Yvette, France, ⁸CSIRO Oceans and Atmosphere, Canberra, ACT, Australia, ⁹Climate Research Division, Environment and Climate Change Canada, Canadian Centre for Climate Modelling and Analysis, Victoria, BC, Canada, ¹⁰Guangdong Province Key Laboratory for Climate Change and Natural Disaster Studies, Zhuhai Key Laboratory of Dynamics Urban Climate and Ecology, School of Atmospheric Sciences, Sun Yat-sen University, Zhuhai, China, ¹¹College of Life and Environmental Sciences, University of Exeter, Exeter, UK, ¹²College of Engineering, Mathematics and Physical Sciences, University of Exeter, Exeter, UK

Supporting Information:

Supporting Information may be found in the online version of this article.

Correspondence to:

J. Xia,
jyxia@des.ecnu.edu.cn

Citation:

Bian, C., Xia, J., Zhang, X., Huang, K., Cui, E., Zhou, J., et al. (2023). Uncertainty and emergent constraints on enhanced ecosystem carbon stock by land greening. *Journal of Advances in Modeling Earth Systems*, 15, e2022MS003397. <https://doi.org/10.1029/2022MS003397>

Received 15 SEP 2022
Accepted 25 APR 2023

Author Contributions:

Conceptualization: Jianyang Xia
Formal analysis: Chenyu Bian
Writing – original draft: Chenyu Bian, Jianyang Xia, Xuanze Zhang, Ying-Ping Wang, Yiqi Luo

Abstract Significant land greening since the 1980s has been detected through satellite observation, forest inventory, and Earth system modeling. However, whether and to what extent global land greening enhances ecosystem carbon stock remains uncertain. Here, using 40 global models, we first detected a positive correlation between the terrestrial ecosystem carbon stock and leaf area index (LAI) over time. Then, we diagnose the source of uncertainty of simulated the sensitivities of ecosystem carbon stock to LAI based on a traceability analysis. We found that the sensitivity of gross primary productivity (GPP) to LAI is the largest contributor to the model uncertainty in more than 60% of the vegetated grids. Using the ensemble of four long-term global data sets of GPP and three satellite LAI products from 1982 to 2014, we provided an emergent constraint on the ecosystem carbon stock increase as 0.75 ± 0.46 kg C m⁻² per unit LAI over global land areas. Furthermore, the biome-based results reveal that the tropical forest regions have the highest inter-model variation and model bias. Overall, this study identifies the uncertainty source and provides constrained estimates of the greening effect on ecosystem carbon stock at the global scale.

Plain Language Summary In the last few decades, we can see that there has been more green land from looking at satellite images, checking forest records, and using computer models. However, we do not know if having more green land is helping the ecosystem store more carbon. This study investigated the greening effect on ecosystem carbon stock among the 40 global models, but this effect varied between models. Therefore, we diagnosed the simulated source of uncertainty based on the traceability analysis framework. Based on satellite-derived data sets, we further constrained the greening effect on ecosystem carbon stock at the global scale. Land greening enhances ecosystem carbon stock, although this increase is highly heterogeneous on a global scale.

1. Introduction

The satellite-observed greening of the land surface has been unequivocal since the early 1980s and widely reported in recent studies mainly as a result of CO₂ fertilization (Chen et al., 2019; Mao et al., 2013; Myneni et al., 1997; Pan et al., 2011; Z. Zhu et al., 2013, 2016). Global land greening suggests more carbon (C) is taken up by land ecosystems due to increased absorption of photosynthetically active radiation (PAR) (Chen et al., 2019; Keenan et al., 2016; Pan et al., 2011; Qian et al., 2010). Multiple lines of evidence have shown that global land greening could slow down the increase in atmospheric carbon dioxide (CO₂) concentration by transferring C from the atmosphere to land (Ballantyne et al., 2017; Chen et al., 2019; Graven et al., 2013; Keenan et al., 2016; Pan et al., 2011; Piao et al., 2020; Qian et al., 2010). However, the mean residence time of C in

© 2023 The Authors. Journal of Advances in Modeling Earth Systems published by Wiley Periodicals LLC on behalf of American Geophysical Union. This is an open access article under the terms of the [Creative Commons Attribution-NonCommercial License](https://creativecommons.org/licenses/by-nc/4.0/), which permits use, distribution and reproduction in any medium, provided the original work is properly cited and is not used for commercial purposes.

Writing – review & editing: Chenyu Bian, Jianyang Xia, Xuanze Zhang, Kun Huang, Erqian Cui, Jian Zhou, Ning Wei, Ying-Ping Wang, Danica Lombardozi, Daniel S. Goll, Jürgen Knauer, Vivek Arora, Wenping Yuan, Stephen Sitch, Pierre Friedlingstein, Yiqi Luo

terrestrial ecosystems ranges from decades in tropical forests (TRFs) to centuries in tundra (J. Wang et al., 2019). Thus, it has been challenging to assess to what extent global land greening has enhanced terrestrial C stock in the past decades.

The ecosystem C stock (ECS) is jointly determined by vegetation productivity and C residence time (Arora et al., 2013; Luo et al., 2003, 2017; Xia et al., 2013; Zhang et al., 2018). However, evidence has revealed contrasting trends in ecosystem productivity (Arora et al., 2013; Friedlingstein et al., 2014; Piao et al., 2020; Winkler, Myneni, Alexandrov, & Brovkin, 2019) and C residence time over the past decades (Brienen et al., 2020; Lu et al., 2018; Wu et al., 2020). On the one hand, land greening is characterized by an increasing leaf area index (LAI), which leads to more active canopy photosynthesis on a global scale. For example, satellite observations and model simulations have shown increasing vegetation productivity (i.e., gross primary productivity, GPP) (Arora et al., 2013; Friedlingstein et al., 2014; Piao et al., 2020; Winkler, Myneni, Alexandrov, & Brovkin, 2019) and peak growth (Huang et al., 2018) since the 1980s. On the other hand, the environmental drivers of land greening, such as rising atmospheric CO₂ concentration and climate warming, could lower C residence time (Brienen et al., 2020; Lu et al., 2018; Wu et al., 2020) in the terrestrial ecosystem by accelerating the turnovers of woody biomass (Yu et al., 2019) and soil organic carbon (Bond-Lamberty et al., 2018; Van Groenigen et al., 2014). Potentially contrasting trends between ecosystem C input and residence time suggest that global land greening could trigger complex plant-soil-atmosphere interactions (Mangan et al., 2010; Piao et al., 2019) and non-uniform effects on ECS across the globe. It remains unclear which processes have dominated ecosystem carbon stock changes due to vegetation greening over the past decades.

Recent advances in data-model integration approaches offer an opportunity to quantify the effect of land greening on ECS on a global scale. By fully coupling the interactions between plants, soil, and atmosphere (Arora et al., 2020), Earth system models (ESMs) are widely used to quantify the greening effect on ECS. Most ESMs currently simulate an increasing trend in carbon uptake (Arora et al., 2013; Friedlingstein et al., 2014; Piao et al., 2020; Winkler, Myneni, Alexandrov, & Brovkin, 2019) and a decreasing trend in ecosystem C residence time (Bond-Lamberty et al., 2018; Van Groenigen et al., 2014; Wu et al., 2020; Yu et al., 2019). However, the simulated magnitude for greening trends and terrestrial C stock by the state-of-the-art ESMs diverged significantly (Luo et al., 2016; Mahowald et al., 2016; Zeng et al., 2016; Z. Zhu et al., 2017). The emergent constraint method developed by Cox et al. (2013) can reduce the inter-model uncertainty by defining an emergent relationship across the multi-model ensemble based on observations. In some previous studies, this approach has been applied to quantify the impacts of global change factors on multiple terrestrial processes, such as GPP (Wenzel et al., 2016), evapotranspiration (Lian et al., 2018), and soil C turnovers (Varney et al., 2020).

The emergent constraint method can reduce inter-model uncertainty by combining the emergent relationship and the corresponding observations (Hall et al., 2019). However, the internal mechanism and source of uncertainty for inter-model remain unclear. In addition, the constrained results have their internal uncertainty due to concerns about the emergent constraints (Winkler, Myneni, & Brovkin, 2019). For example, the emergent relationship is derived from the model ensemble, and thus it could be misleading if the model ensemble has some systematic error (Eyring et al., 2019). For the land C cycle, the traceability analysis framework can trace the inter-model uncertainty by decomposing a complex land model to its traceable components based on the C cycle fundamental properties (Luo et al., 2017; Xia et al., 2013). This framework has been widely used for tracing and evaluating the model uncertainty (Wei, Xia, Zhou, et al., 2022; S. Zhou et al., 2018; J. Zhou et al., 2021) at both site and global scales. Therefore, combining the emergent constraint and traceability analysis can help us constrain the inter-model uncertainty and further understand the effects of vegetation on C stock in global models.

In this study, we use the modeling outputs from the fifth and sixth phases of Coupled Model Intercomparison Projects (CMIPs) (i.e., CMIP5 and CMIP6; Tables S1 and S2 in Supporting Information S1) and the Trends in Net Land-Atmosphere Carbon Exchanges project (TRENDY-v9; Table S3 in Supporting Information S1) to investigate the greening effect (i.e., LAI) on ECS since the 1980s. Then, we diagnose the main contributor to the large spread of the simulated greening effect on C stock among different models based on the traceability analysis method. After that, by building an emergent relationship between the greening effects on GPP and ECS, we constrain the estimated greening effect on ECS based on the long-term global observations using an emergent constraint approach. We explore the spatial pattern of the greening effect on ECS using multiple sources of data sets. Lastly, we compare the inter-model variation and model bias of the greening effect on C stock among different biomes.

2. Materials and Methods

2.1. The Model Intercomparison Projects

In this study, we evaluated the greening effect on ecosystem carbon stock based on the model simulation results among the three MIPs (i.e., CMIP5, CMIP6, and TRENDY-v9). The CMIPs were established to compare the intermodel climate variability and fill the understanding gap of land-atmospheric carbon exchange and feedback with the climate system (Eyring et al., 2016; Taylor et al., 2012). To improve predictions of the terrestrial ecosystem to climate change, the land carbon cycle models have gradually incorporated more and more new processes (Prentice et al., 2015). In the meantime, it also leads to large variations in the simulations and predictions across models and MIPs (S. Zhou et al., 2018). This study uses two generations of CMIPs (CMIP5 and CMIP6) to estimate the greening effects on ECS. There are two primary reasons to include different numbers of models: (a) the variant label of ESMs with “r1i1p1” for CMIP5 and “r1i1p1f1” for CMIP6; (b) a model can be selected if it provides all the diagnostic variables that are required for this study. The variables used to evaluate greening effects include carbon fluxes (i.e., net primary production (npp), gross primary production (gpp), net ecosystem production (nep), and heterotrophic respiration (rh)), leaf area index (lai), carbon pools (cVeg, cLitter, and cSoil), near-surface temperature (tas) and precipitation (pr). Based on these two requirements, a total of 16 ESMs for CMIP5 and 12 ESMs for CMIP6 were selected. More details about the variables used in each model are shown in Tables S1 and S2 in Supporting Information S1. Thus, this study selected outputs of 28 models from the CMIP historical simulations. The CMIP historical simulations of climate change are forced by common data sets (i.e., CO₂ concentration and land use) that largely based on observations. Thus, the historical simulations have included the impact of land-use and land cover change on ECS (Lawrence et al., 2016). In general, they serve as a benchmark for assessing model performance through evaluation with observations (Eyring et al., 2016).

CMIP5. The fifth phase of the Coupled Model Intercomparison Project (CMIP5) mainly focused on the gaps in understanding past and future climate change by performing a suite of climate simulations (Taylor et al., 2012). It contributed from various modeling centers involving the Fifth Assessment Report (AR5) of the International Panel on Climate Change (IPCC). More than 50 models from 20 modeling groups have attended CMIP5. The simulations include two types of climate change experiments: long-term and near-term integrations (Taylor et al., 2012). We only used the long-term history simulation results in this study. The simulation data sets are available from the CMIP5 archive (<http://cmip-pcmdi.llnl.gov/cmip5/>). We selected 16 models from the historical model scenarios (Table S1 in Supporting Information S1).

CMIP6. The Coupled Model Intercomparison Project Phase 6 (CMIP6) aims to address a wide variety of science questions from a spread of scientific research communities (Eyring et al., 2016; Meehl et al., 2000, 2005, 2014). CMIP6 has adopted a more federated structure and subsequent phase. The core experiments include DECK (Diagnostic, Evaluation, and Characterization of Klima) experiments and historical simulations (Eyring et al., 2016). This study selected 12 models (Table S2 in Supporting Information S1) from the historical simulations based on the data availability (<https://pcmdi.llnl.gov/CMIP6/>).

TRENDY. This study used an ensemble of 12 processed-based dynamic global vegetation models (DGVMs), including CABLE-POP, CLASSIC, CLM5.0, IBIS, JSBACH, JULES-ES, LPX-Bern, OCN, ORCHIDEE-CNP, ORCHIDEEv3, SDGVM, and VISIT from the Trends in Net Land-Atmosphere Carbon Exchanges project (TRENDY-v9; Friedlingstein et al., 2020) for 1982–2019 (Table S3 in Supporting Information S1). These models have performed the same set of factorial simulations following a standard protocol. Therefore, it can avoid some uncertainties due to climate variability. This study used the output from “S3” simulations under the scenarios with time-varying atmospheric CO₂ and changing climate and land use. The annual time series of global atmospheric CO₂ is derived from ice core CO₂ data merged with NOAA annual resolution for 1700–2019. Either monthly CRU or 6-hourly CRU-JRA55 with a 0.5° × 0.5° resolution can be used to force these DGVMs. DGVMs are spun-up to steady-state by recycling climate mean and variability from 1901 to 1920 and an atmospheric CO₂ concentration of 276.59 ppm (i.e., 1700 level).

We summed all the carbon pools as ecosystem carbon stock for each model. All the model output variables from three MIPs were linearly interpolated from their native resolution to a standard 0.5° × 0.5° grid on a global scale. In addition, we only selected the temporal period after 1982 (1982–2005 for CMIP5; and 1982–2014 for CMIP6; 1982–2019 for TRENDY-v9), considering global greening has been detected since the early 1980s and the satellite-observed LAI data sets are available from 1982.

2.2. Observation Data Sets

Satellite-derived data products provide consistent estimates of LAI and GPP across large spatial and temporal ranges. These data sets have also been widely used for monitoring terrestrial vegetation growth and ecosystem productivity. In this study, three available LAI and four GPP data sets are integrated to access the greening effect on ECS. In addition, two independent data sets, which include eddy-flux observations and the vegetation optical depth (VOD) derived aboveground biomass (AGB), are used to validate the constrained spatial pattern further.

2.2.1. Satellite-Observed LAI Products

The Global Inventory Modeling and Mapping Studies (GIMMS) LAI3g product (Z. Zhu et al., 2013) was generated by Feed-Forward Neural Network (FFNN) algorithm based on NDVI3g data from July 1981 to December 2011. It provides global data at a spatial resolution of $1/12^\circ$ and a temporal resolution of half a month. The long-term GLOBMAP LAI product was generated by a combination of AVHRR LAI (1981–2000) and MODIS LAI (2000–2011) (Y. Liu et al., 2012). By establishing the relationship between AVHRR observations and MODIS LAI during the overlapped period (2000–2006), the AVHRR LAI can be retrieved back to 1981. The temporal resolution of this data set is half a month and eight days in 1981–2000 and 2001–2011, respectively. The spatial resolution is 8 km. The GLASS LAI product was estimated from MODIS and AVHRR time-series remote sensing data using the General Regression Neural Networks (GRNNs) approach. The GLASS LAI product provides a geographic projection at the resolution of 0.05° from 1981 to 1999 and a sinusoidal projection at 1 km from 2000 to 2014 (Xiao et al., 2013, 2016). The three satellite-observed products were re-sampled into $0.5^\circ \times 0.5^\circ$ special resolution using the nearest neighbor algorithm for the period 1982–2014.

2.2.2. Satellite-Derived GPP Data Sets

This study uses four satellite data-driven long-term global GPP data sets, including EC-LUE GPP, GPP_{Enh} , P-Model GPP, and RS-LUE GPP (described below). We linearly interpolated all the four GPP data sets from their native resolution to a standard $0.5^\circ \times 0.5^\circ$ spatial resolution and further selected the data sets from 1982 to 2014 to match the LAI data sets.

EC-LUE GPP. The GPP data set was generated from the revised light-use efficiency (LUE) model, EC-LUE, by integrating the regulations of several environmental variables, which include CO_2 concentration, radiation, and atmospheric vapor pressure deficit (VPD), and driven by four variables: normalized difference vegetation (NDVI), PAR, air temperature, and the Bowen ratio of sensible to latent heat flux (Yuan et al., 2007, 2010). The EC-LUE model is based on two fundamental assumptions: (a) the fraction of absorbed PAR (fPAR) has a linear relationship with NDVI; (b) the LUE is limited by air temperature or soil moisture (Yuan et al., 2007). The revised EC-LUE model performed well in the simulation of global GPP and was validated and compared by some other studies (Zheng et al., 2020). The temporal resolution of this data set is eight days for 1982–2018, and the spatial resolution is 0.05° .

GPP_{Enh}. The GPP_{Enh} data set was generated based on an enhanced remote sensing LUE model (Madani et al., 2017, 2020). The LUE model which provides enhanced GPP estimates in this study as follows: $GPP_{Enh} = FPAR \times PAR \times LUE_{opt} \times fVPD \times fSM \times fT_{min}$, where $fVPD$, fSM , and fT_{min} represents the water and temperature environmental constraint functions. The optimized LUE was extrapolated to the global domain based on a generalized additive model GAM framework (Hastie & Tibshirani, 1986). Global monthly GIMMS3g FPAR (Z. Zhu et al., 2013), meteorological data sets from Modern-Era Retrospective analysis for Research and Applications, Version2 (MERRA-2; Gelaro et al., 2017), and geospatial information are the primary input to drive the LUE model. More details about this data set can be found in Madani et al. (2017, 2020). It provides global data at a spatial resolution of 8 km and a monthly temporal resolution from 1982 to 2016.

P-model GPP. The P-model is also a LUE model based on an optimality principle that predicts stomatal conductance and foliar photosynthesis (H. Wang et al., 2017). This study used the estimated GPP on a global scale developed by B. D. Stocker et al. (2018, 2019) with the Seasonal optimization of fixation and uptake of nitrogen (SOFUN v1.1.0, B. Stocker, 2018) modeling framework. In the P-model, GIMMS3g FPAR data sets drive the simulations of GPP on a global scale from 1982 to 2016. A set of empirical soil moisture stress functions ($GPP = \beta(\theta)GPP_{mod}$) are used to correct the simulated GPP. The simulations of s1b results are used in this study. Where s1b represents using parameters of β_b (the intermediate sensitivity and distinguishing

parameters between woody and herbaceous vegetation) to estimate the uncertainty in the sensitivity of $\beta(\theta)$. The temporal resolution of the GPP data set provided by the P-model is daily for 1982–2016, and the spatial resolution is 0.5° .

RS-LUE GPP. The remote-sensing-based LUE (RS-LUE) model can estimate GPP fluxes based on the MODIS GPP algorithm (Kolby Smith et al., 2016; Running et al., 2004) as $GPP = FPAR \times PAR \times LUE_{max} \times f(T_{min}) \times f(VPD)$. The FPAR is a satellite-derived fraction of PAR absorbed by vegetation, which is based on the GIMMS3g using a neural network algorithm (Z. Zhu et al., 2013). PAR is incoming PAR. LUE_{max} represents the maximum LUE. The functions of $f(T_{min})$ and $f(VPD)$ represent the environmental function for minimum temperature and VPD, respectively. In this study, we used an updated version extending for 1982–2016 (Version 4) with the CRUNCEP P1 Standard run (O’Sullivan et al., 2020). The spatial resolution is $0.5^\circ \times 0.5^\circ$ grid, and the temporal resolution is monthly.

2.2.3. Data-Oriented Aboveground Biomass Carbon and FLUXNET Data

The passive microwave-based global AGB carbon product (version 1.0; Y. Y. Liu et al., 2015) is derived from a harmonized time series of VOD from 1993 to 2012. The passive microwave-based AGB data set provided annual estimates with a spatial resolution of 0.25° , respectively. The reported uncertainty of the passive microwave-based AGB in each grids cell was less than 30% (Saatchi et al., 2011). In this study, we re-sampled the AGB data from the spatial resolution of 0.25° – 0.5° .

The daily eddy covariance NEE data were obtained from FLUXNET2015 (Tier1) data sets (<http://fluxnet.fluxdata.org/data/fluxnet2015-dataset/>), which is an openly available database that offers an observation of carbon fluxes between ecosystems and the atmosphere. These data included in the data sets are collected at sites from multiple flux networks worldwide (<https://fluxnet.fluxdata.org/>) and were pre-filtered to exclude the low turbulence conditions to meet the requirement of the eddy-covariance technique, as described in Papale et al. (2006). A total of 82 flux sites (Table S4 in Supporting Information S1 for a full list, which has at least 5-year consistent data) with 925 site-years of NEE data were used in this study. However, considering flux sites did not include corresponding LAI data sets, we extracted the satellite observed LAI values within a 3×3 pixel window around the site based on the original resolution for each of the three LAI products (Table S5 in Supporting Information S1) as similar to the previous study (Huang et al., 2019). Then we use the average of 3×3 pixels based on the ensemble of three LAI products to represent the LAI values in each site. Here we use the positive sign convention for land carbon uptake, that is: $NEP = -NEE$, and calculated the sensitivity of NEP to LAI-based observed data sets (Table S4 in Supporting Information S1).

2.2.4. Biome Classification

We evaluated the greening effect on C stock at the biome-level by constructing a common biome mask. The biome map was based on the MODIS/TERRA-AQUA land cover product (MCD12C1) Collection 5.1 (Friedl et al., 2010). We masked water, permanent snow and ice, and barren regions first. We assigned one of the remaining land cover types to a $0.5^\circ \times 0.5^\circ$ grid cell by taking the most common land cover from the original underlying $0.05^\circ \times 0.05^\circ$. Then each 0.5° grid was further classified into one of eight biomes, following the details in Todd-Brown et al. (2013) as tundra, boreal forest (BOF), TRF, temperate forest (TEF), shrubland, grassland and savannas, cropland and urban, or wetlands (Figure S1 in Supporting Information S1).

2.3. Traceability Analysis on the Modeled Sensitivity of C Stock to LAI

2.3.1. Traceability Analysis Framework on C Stock

We conducted a traceability analysis to further explain the wide spread of sensitivities of ecosystem carbon stock to LAI among the 40 global models from three MIPs based on the Traceability analysis system for Model Evaluation (TraceME v1.0; J. Zhou et al., 2021). The TraceME system is based on the traceability analysis framework (Xia et al., 2013) to identify the inter-model source of uncertainties in ecosystem carbon stock to its components. This traceability framework has been widely used and developed in diagnosing the causes of differences in simulated terrestrial carbon cycle among models (Jiang et al., 2017; Luo et al., 2017; Wei, Xia, Zhou, et al., 2022; Xia et al., 2013; S. Zhou et al., 2018). The traceability analysis method used in this study is briefly described below.

ECS is jointly determined by ecosystem carbon influx (e.g., NPP) and ecosystem C residence time (τ_E) (Xia et al., 2013):

$$\text{ECS} = \tau_E \times \text{NPP} \quad (1)$$

The ecosystem C residence time (Lu et al., 2018) in Equation 1 can be calculated by the following equation:

$$\tau_E = \text{ECS}/R_h \quad (2)$$

where ECS is the current C stock, which equals the sum of all C pools in each model. R_h represents the carbon losses through heterotrophic respiration. Generally, τ_E are directly available based on each model structure and the environmental scalars (i.e., ξ):

$$\tau_E = \tau'_E \xi^{-1} \quad (3)$$

where τ'_E represents ecosystem baseline C residence time. The term τ'_E usually preset based on the model-specific structure and parameters (i.e., C transfer coefficients among different C pools, C allocation coefficients, and decomposition coefficients); ξ is an environmental scalar that reflects the environmental regulators on τ'_E , especially the temperature (ξ_T) and water (ξ_W) scalar. In this study, we only considered the effect of temperature (ξ_T) and water (ξ_W) as similar to the previous studies (Jiang et al., 2017; Wei, Xia, Zhou, et al., 2022; Xia et al., 2013; S. Zhou et al., 2018; J. Zhou et al., 2021):

$$\xi = \xi_T \xi_W \quad (4)$$

The term ξ_T and ξ_W can be estimated by mean annual temperature (T) and annual total precipitation (W) (S. Zhou et al., 2018) as:

$$\xi_T = Q_{10}^{[(T-T_0)/10]} \quad (5)$$

$$\xi_W = \frac{W}{W_0} \quad (6)$$

where Q_{10} is a parameter that represents the temperature sensitivity of ecosystem respiration. The terms T_0 and W_0 represent the reference temperature and precipitation, respectively. In this study, T_0 and W_0 were set as the maximum values of annual temperature and precipitation in the simulation period for each model.

In addition, NPP in Equation 1 can be decomposed into gross primary production (GPP) and carbon use efficiency (CUE) (Xia et al., 2017):

$$\text{NPP} = \text{CUE} \times \text{GPP} \quad (7)$$

2.3.2. Source of Uncertainty on Modeled Sensitivity of ECS to LAI

Applying the traceability analysis framework, we first decomposed the ECS to its traceable component. Then, we quantified the contributions of each traceable component to the uncertainty of modeled sensitivity of ECS to LAI based on the hierarchical partitioning method (Chevan & Sutherland, 1991; Murray & Conner, 2009). This method can be used to calculate the independent effect of each explanatory variable on a single dependent variable. For a given dependent variable (y) and k explanatory variables ($x_1, x_2, x_3, \dots, x_k$), there would be 2^k different combinations of explanatory variables. For example, when $k = 3$, there are $2^3 = 8$ numbers are required. The eight numbers are indexed as $X_0, X_1, X_2, X_3, X_{12}, X_{13}, X_{23}$, and X_{123} . Each subscript represents the combination of the concluded explanatory variables (i.e., X_{12} represents the combination of x_1 and x_2 , while X_0 is a null number). The independent effect of each explanatory variable x_l ($l = 1, 2, 3, \dots, k$) on a single dependent variable y can be calculated by comparing the fit of all nested models (2^k) lacking that variable based on the hierarchical ordering (Chevan & Sutherland, 1991; Murray & Conner, 2009):

$$I_{x_i} = \sum_{i=0}^{k-1} \frac{\sum (r_{y,x_i x_h}^2 - r_{y,x_h}^2)}{k} \binom{k-1}{i} \quad (8)$$

where x_h is any subset of explanatory variables excluding x_i (Chevan & Sutherland, 1991; Murray & Conner, 2009). The relative independent contribution (RI_{x_i}) can be further calculated as:

$$RI_{x_i} = \frac{I_{x_i}}{\sum_{i=1}^k I_{x_i}} \quad (9)$$

We converted all the traceable components to their logarithmic form to ensure the formulations could be expressed in sum form. Then, we calculated the sensitivity of each component to LAI (e.g., $\partial \ln(\text{ECS})/\partial \text{LAI}$, $\partial \ln(\text{NPP})/\partial \text{LAI}$, $\partial \ln(\text{CUE})/\partial \text{LAI}$, $\partial \ln(\text{GPP})/\partial \text{LAI}$, $\partial \ln(\tau_E)/\partial \text{LAI}$, $\partial \ln(\tau'_E)/\partial \text{LAI}$, $\partial \ln(\xi)/\partial \text{LAI}$, $\partial \ln(\xi_T)/\partial \text{LAI}$, $\partial \ln(\xi_W)/\partial \text{LAI}$). After that, we conducted the hierarchical partitioning analysis using the “hier.part” package in R (version 4.2.1), which is based on a linear regression by hierarchical decomposition of goodness-of-fit measures of regressions using all subsets of predictors in the data set.

2.4. Emergent Constraint Method

The simulation results of ESMs often exhibit significant differences due to their complexity and incorporation of many processes. It is difficult to understand the climate system or predict future changes accurately. The terrestrial ecosystem, which sequesters about one-third of anthropogenic CO₂ emissions each year, acts as a substantial carbon sink and plays a vital role in climate change (Friedlingstein et al., 2020; Le Quéré et al., 2018). Therefore, improving our understanding of the terrestrial ecosystem is important to reduce current uncertainties in projections of future change. In a previous study, Cox et al. (2013) have developed an “emergent constraint” method to reduce the uncertainty of future climate impact on the tropical C cycle. This approach defines an emergent relationship among multi-model outputs and uses one observable variable to constrain another that could not be observed or measured directly (Eyring et al., 2019; Hall et al., 2019). Here we use a similar constrained approach to evaluate the greening effect on ECS. To obtain model-specific greening effect on GPP and C stock, the monthly model output data were first time-averaged to yearly over the study period. Then, for each model, the sensitivities of GPP and C stock to LAI are calculated based on the globally averaged values. We established an emergent relationship between the sensitivities of GPP and C stock to LAI based on the ensemble of global models in CMIP5, CMIP6, and TRENDY (1982–2005 for CMIP5; and 1982–2014 for CMIP6; 1982–2019 for TRENDY-v9). We compared the different GPP-LAI sensitivities by analyzing all the combinations of four GPP and three LAI products ($n = 12$; Figure S2 in Supporting Information S1). The constrained results produced by different GPP and LAI combinations are highly uncertain (Figure S3 in Supporting Information S1). Thus, the multiple data sets of GPP and LAI were integrated as a constrain to reduce the possible observational uncertainty. In addition, we also calculated the greening effect on GPP and C stock for each pixel for each model to do the spatial emergent constraint.

A linear least-squares regression model was first built between the partial sensitivity of ECS to LAI ($\partial \text{ECS}/\partial \text{LAI}$) and the partial sensitivity of GPP to LAI ($\partial \text{GPP}/\partial \text{LAI}$) across the models:

$$\hat{y}_i = a + bx_i + \varepsilon_i \quad (10)$$

Let the least-squares for y_i involves minimizing, then the least-squares error of the regression model can be calculated as:

$$s^2 = \frac{1}{N-2} \sum_{i=1}^N \{y_i - \hat{y}_i\}^2 \quad (11)$$

Then for a given x , the “prediction error” is:

$$\sigma_f(x) = s \sqrt{1 + \frac{1}{N} + \frac{\{x - \bar{x}\}^2}{N\sigma_x^2}} \quad (12)$$

where \bar{x} is the mean value of a series of x , and σ_x^2 is the variance of x , which can be calculated as:

$$\sigma_x^2 = \frac{\sum_{i=1}^N \{x_i - \bar{x}\}^2}{N} \quad (13)$$

The probability density function of the predicted variable \hat{y} given x is provided by the Cox et al. (2013) as:

$$P(\hat{y}|x) = \frac{1}{\sqrt{2\pi\sigma_f^2}} \exp\left\{-\frac{(y_i - \hat{y}_i)^2}{2\sigma_f^2}\right\} \quad (14)$$

where $\sigma_f = \sigma_f(x)$, as described above.

Finally, for a given observation-based probability distribution function (PDF) $P(x)$ and a model-based PDF $P(\hat{y}|x)$, the PDF of the emergent constraint on y is:

$$P(y) = \int_{-\infty}^{\infty} P(\hat{y}|x)P(x)dx \quad (15)$$

3. Results

3.1. Inter-Model Variation of the Greening Effect on Ecosystem C Stock

The multi-model ensemble of global ECS was positively correlated with global mean LAI in CMIP5 ($n = 16$, $R^2 = 0.80$, $P < 0.001$; Figure 1a) from 1982 to 2005, CMIP6 ($n = 12$, $R^2 = 0.95$, $P < 0.001$; Figure 1b) from 1982 to 2014, and TRENDY ($n = 12$, $R^2 = 0.96$, $P < 0.001$; Figure 1c) from 1982 to 2019. Such a significantly positive sensitivity was found in 11 out of 16 models in CMIP5 and all models in CMIP6 and TRENDY (Figure 1d). The sensitivity of C stock to per unit of LAI changes greatly varied among the models, ranging from -0.59 to 4.35 kg C m⁻² per m² m⁻² in CMIP5, from 0.12 to 3.79 kg C m⁻² per m² m⁻² in CMIP6, and from 0.36 to 4.88 kg C m⁻² per m² m⁻² in TRENDY (Figure 1d; Table S6 in Supporting Information S1). Thus, the CMIP5 models have the largest variation of the sensitivity of C stock to per unit of LAI change (with a standard deviation of 1.50 kg C m⁻² per m² m⁻²), followed by the TRENDY (a standard deviation of 1.20 kg C m⁻² per m² m⁻²) and CMIP6 (a standard deviation of 1.11 kg C m⁻² per m² m⁻²) models (Figure 1d). The spatial distribution with greater inter-model variation of the sensitivity of C stock to LAI among the 40 models were mainly located in TRF, boreal, and shrubland regions (Figure 1e).

The inter-model variation in the sensitivity of C stock to LAI was jointly contributed by C stock and LAI. For example, among the 16 ESMs in CMIP5, the global multi-year mean of C stock ranges from 5.33 kg C m⁻² for CESM1-WACCM to 23.28 kg C m⁻² for GFDL-ESM2G (Figure S4a in Supporting Information S1), while LAI varies from 1.53 m² m⁻² for CanESM2 to 3.38 m² m⁻² for MPI-ESM1 (Figure S5a in Supporting Information S1). For the 12 ESMs in CMIP6, C stock varies from 5.36 to 65.09 kg C m⁻² (Figure S4a in Supporting Information S1), while LAI changes from 1.33 to 2.21 m² m⁻² (Figure S5a in Supporting Information S1). For the 12 DGVMs in TRENDY models, C stock varies from 7.22 to 58.58 kg C m⁻² (Figure S4a in Supporting Information S1), while LAI changes from 1.46 to 4.03 m² m⁻² (Figure S5a in Supporting Information S1). The ensemble means of global multi-year averaged LAI in CMIP6 (1.79 m² m⁻²) is much less than that for CMIP5 (2.30 m² m⁻²) or TRENDY (2.45 m² m⁻²). Only IPSL-CM5A-LR and NorESM1-ME simulated a negative correlation between LAI and C stock in CMIP5 (Figure 1d). The simulated LAI by IPSL-CM5A-LR (Figure S5b in Supporting Information S1) and the simulated C stock by CESM1-WACCM and NorESM1-ME (Figure S4b in Supporting Information S1) decreased over time.

3.2. Trace the Source of Uncertainty in Modeled Sensitivity of Ecosystem Carbon Stock to LAI

The variation in modeled sensitivity of ECS to LAI is decomposed into several traceable components' sensitivity to LAI based on the traceability analysis framework in temporal and spatial scales (1982–2005 for CMIP5; and 1982–2014 for CMIP6; 1982–2019 for TRENDY-v9; Figure 2). The terms $\partial \ln(\text{NPP})/\partial \text{LAI}$ and $\partial \ln(\tau_E)/\partial \text{LAI}$ contribute equally (50%) to the across-model variance in the sensitivity of C stock to LAI in all three MIPs

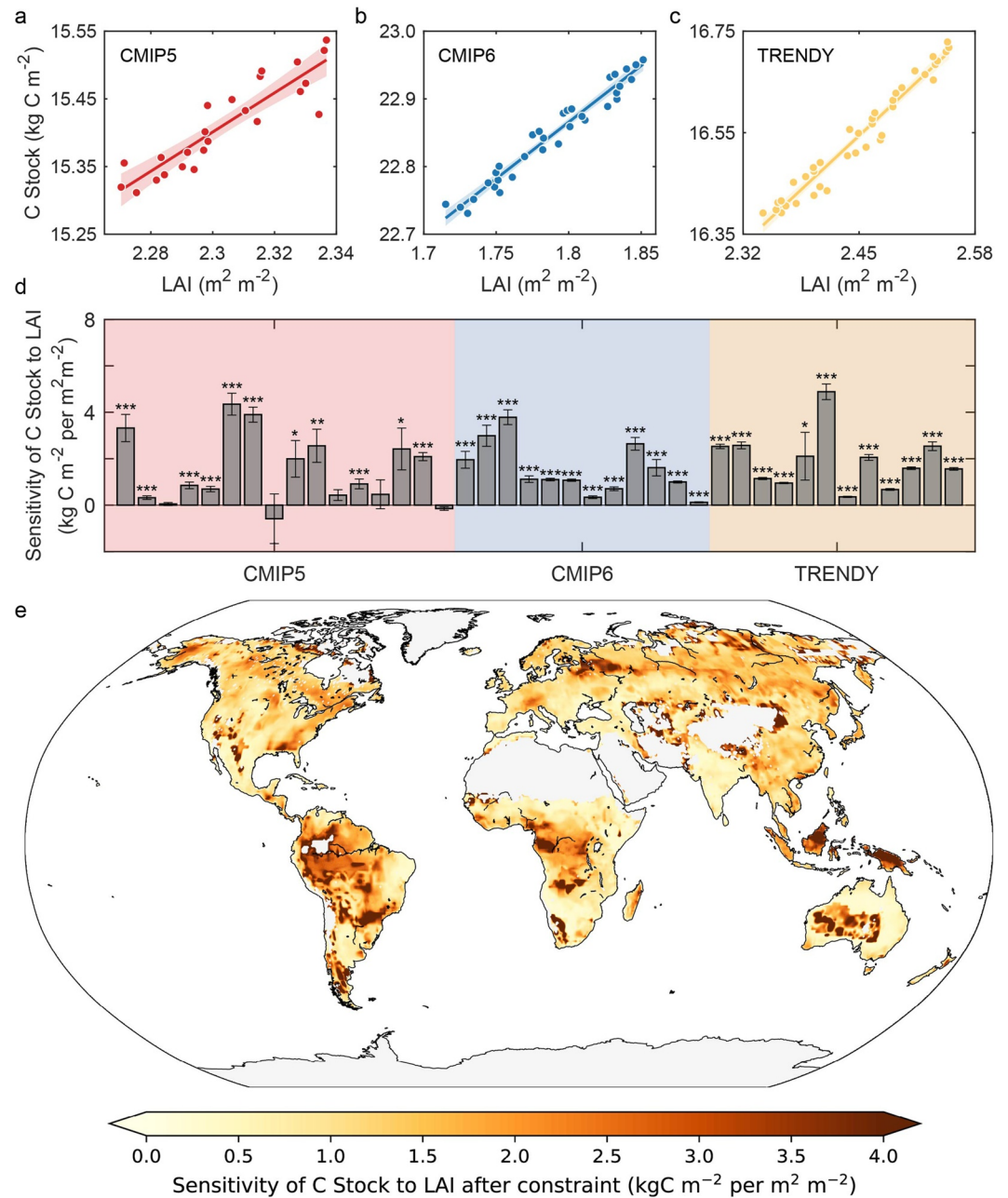


Figure 1. Comparison of the sensitivity of ecosystem carbon stock to leaf area index (LAI) among Coupled Model Intercomparison Projects and TRENDY models. (a–c) Temporal relationship between ecosystem C stock and LAI based on the model ensemble of Coupled Model Intercomparison Project (CMIP5) (a), Coupled Model Intercomparison Project Phase 6 (CMIP6) (b) and TRENDY (c). Each scatter represents an individual year of LAI and C stock for the model ensemble results and the straight lines represent the linear regression for the model ensemble with red, blue, and yellow indicating CMIP5, CMIP6, and TRENDY, respectively. Panel (d) shows the sensitivities of C stock to per unit LAI change in 40 models for the three MIPs. Each bar represents one model. The error bars indicate the mean \pm standard error (i.e., SE) of the sensitivity of C stock to LAI. The asterisks indicate the trend is statistically significant using a *t*-test, *** represents $P < 0.001$, ** represents $P < 0.01$, * represents $P < 0.05$. (e) The spatial distribution of standard deviation in the sensitivity of C stock to LAI among the 40 models.

based on the results of temporal dynamics. The modeled variation of $\partial \ln(\text{NPP}) / \partial \text{LAI}$ can be decomposed into $\partial \ln(\text{GPP}) / \partial \text{LAI}$ and $\partial \ln(\text{CUE}) / \partial \text{LAI}$. The contributions of $\partial \ln(\text{GPP}) / \partial \text{LAI}$ to the $\partial \ln(\text{NPP}) / \partial \text{LAI}$ variation is 71% for CMIP5, 77% for CMIP6, 99% for TRENDY, and 90% for the three MIPs, while the contributions of

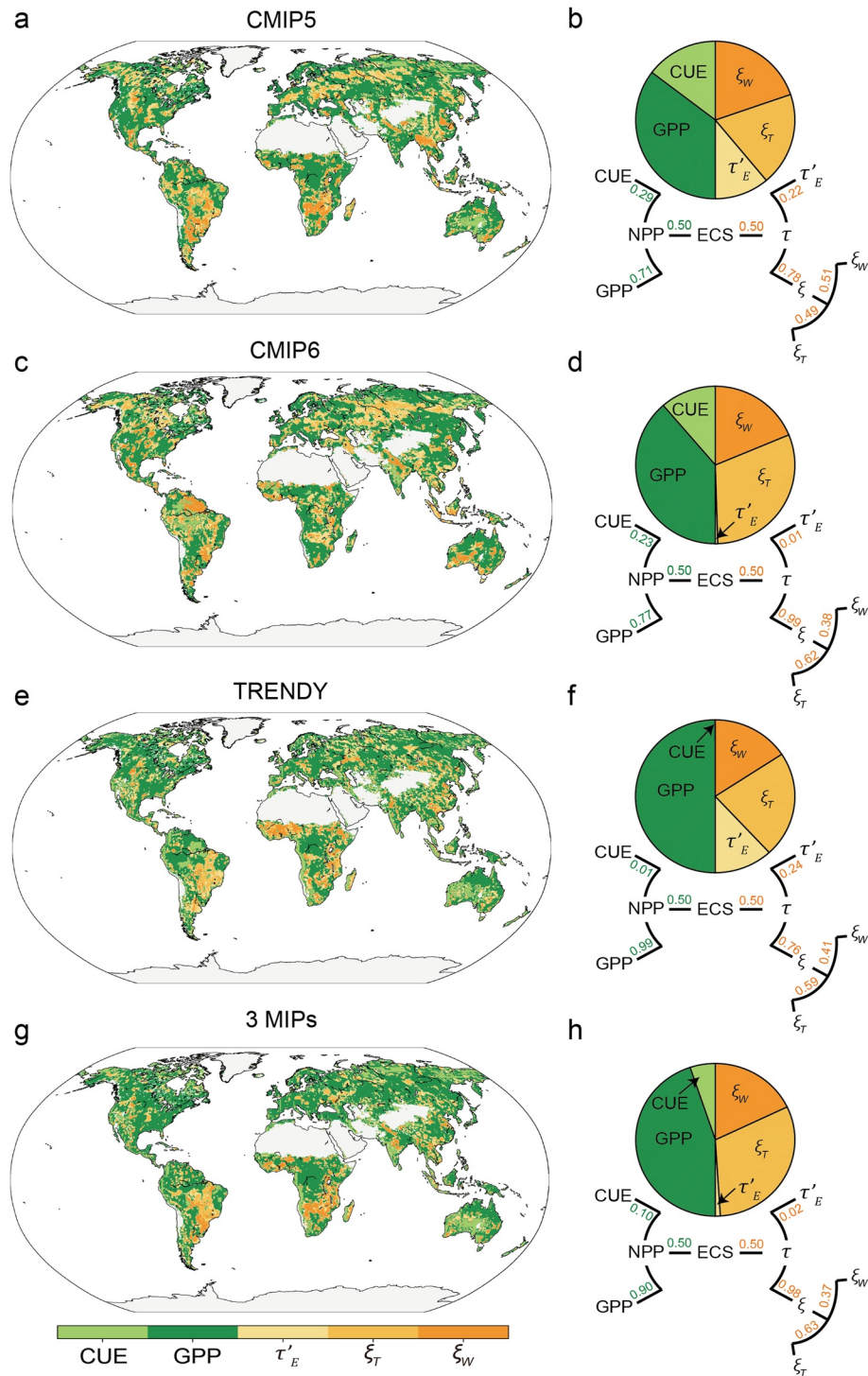


Figure 2. Variance decomposition of the sensitivity of ecosystem carbon stock to leaf area index (LAI) for Coupled Model Intercomparison Project (a, b), Coupled Model Intercomparison Project Phase 6 (c, d), TRENDY (e, f), and all the models from three MIPs (g, h). The left global maps show the spatial distribution of the dominant variable for the variation. The pie plots represent the attribution of variance for each component sensitivity to LAI. The right panels show the hierarchical decomposition of ecosystem carbon stock into its components. We first converted all the traceable components to its logarithmic form, and further quantified the contributions of each traceable component to the uncertainty of modeled sensitivity of ecosystem C stock to LAI (see Section 2.3.2). The variation of $\partial \ln(\text{ECS})/\partial \text{LAI}$ is decomposed to $\partial \ln(\text{NPP})/\partial \text{LAI}$ and $\partial \ln(\tau_E)/\partial \text{LAI}$. And then, variation of $\partial \ln(\text{NPP})/\partial \text{LAI}$ is decomposed into $\partial \ln(\text{GPP})/\partial \text{LAI}$ and $\partial \ln(\text{CUE})/\partial \text{LAI}$, while $\partial \ln(\tau_E)/\partial \text{LAI}$ could be decomposed into $\partial \ln(\tau'_E)/\partial \text{LAI}$ and $\partial \ln(\xi)/\partial \text{LAI}$. $\partial \ln(\xi)/\partial \text{LAI}$ could further decomposed to $\partial \ln(\xi_T)/\partial \text{LAI}$ and $\partial \ln(\xi_W)/\partial \text{LAI}$. The symbols in the figure is: C residence time (τ), baseline C residence time (τ'_E), environmental scalar (ξ), temperature scalar (ξ_T) and water scalar (ξ_W).

$\partial \ln(\text{CUE})/\partial \text{LAI}$ to the $\partial \ln(\text{NPP})/\partial \text{LAI}$ variation is 29% for CMIP5, 23% for CMIP6, 1% for TRENDY, and 10% for all the global models from the three MIPs. It suggests that the variation in $\partial \ln(\text{GPP})/\partial \text{LAI}$ represents the largest uncertainty source in the modeled sensitivity of NPP to LAI. By decomposing the variation of $\partial \ln(\tau_E)/\partial \text{LAI}$ into $\partial \ln(\tau'_E)/\partial \text{LAI}$ and $\partial \ln(\xi)/\partial \text{LAI}$, we found that the contribution of $\partial \ln(\tau'_E)/\partial \text{LAI}$ to $\partial \ln(\tau_E)/\partial \text{LAI}$ is smaller than that of $\partial \ln(\xi)/\partial \text{LAI}$. Specifically, the contributions of $\partial \ln(\tau'_E)/\partial \text{LAI}$ to the $\partial \ln(\tau_E)/\partial \text{LAI}$ variation is 22% for CMIP5, 1% for CMIP6, 24% for TRENDY, and 2% for the three MIPs, while the contributions of $\partial \ln(\xi)/\partial \text{LAI}$ to the $\partial \ln(\tau_E)/\partial \text{LAI}$ variation is 78% for CMIP5, 99% for CMIP6, 76% for TRENDY, and 98% for the three MIPs. In addition, $\partial \ln(\xi_T)/\partial \text{LAI}$ has a greater contribution to the $\partial \ln(\xi)/\partial \text{LAI}$ compared with $\partial \ln(\xi_W)/\partial \text{LAI}$ for CMIP6 (62%), TRENDY (59%), and all the three MIPs combined (63%), but a smaller contribution for CMIP5 (49%) (Figures 2b, 2d, 2f, and 2h).

We further detect each traceable component's contribution to the variation of the greening effect on ECS across models on a spatial scale. The contribution of each component was calculated for each grid. The component which made the greatest contribution to the variation in $\partial \ln(\text{ECS})/\partial \text{LAI}$ was identified as the dominant uncertainty source (Figures 2a, 2c, 2e, and 2g). The results showed that $\partial \ln(\text{GPP})/\partial \text{LAI}$ was the main uncertainty contributor whether for CMIP5 (at 62.0% vegetated land grid), CMIP6 (60.1%), TRENDY (56.3%), or all three MIPs (60.4%). The spatial distribution of the other contributors varies greatly among the three MIPs. For CMIP5 and CMIP6, the contribution of $\partial \ln(\tau'_E)/\partial \text{LAI}$ was mainly located in central Siberia; while for TRENDY and the ensemble of three MIPs, the contribution of $\partial \ln(\tau'_E)/\partial \text{LAI}$ was mainly located in Brazil regions.

3.3. Observational-Based Greening Effect on Gross Primary Production

We examined the inter-annual covariance between satellite-derived GPP (Figure S6 in Supporting Information S1) and LAI (Figure S7 in Supporting Information S1) in each vegetated land grid cell between 1982 and 2014. About 68.8% of vegetated land grids showed a significant positive correlation between GPP and LAI (Figure 3; Figure S8 in Supporting Information S1). The mean sensitivity of GPP to per-unit change of LAI (i.e., the slope of GPP-LAI correlations) across all land grids was $297.91 \pm 267.41 \text{ g C m}^{-2} \text{ yr}^{-1} \text{ per m}^2 \text{ m}^{-2}$, which was significantly larger than zero (t -test, $P < 0.05$; Figure 3b). Then, we classified the observed sensitivity of GPP to LAI change into eight biomes based on the MODIS/TERRA-AQUA land cover product (MCD12C1; Friedl et al., 2010) Collection 5.1 (Figure S1 in Supporting Information S1). Among the eight biomes, as shown in Figure 3c, shrubland had the largest sensitivity of GPP to per unit change in LAI (482.01 ± 322.33), followed by grassland (403.11 ± 292.10), cropland (379.72 ± 244.75), tundra (250.25 ± 204.63), BOF (185.74 ± 126.25), TEFs (154.93 ± 112.21), wetlands (148.34 ± 140.35), and TRFs ($14.16 \pm 93.09 \text{ g C m}^{-2} \text{ yr}^{-1} \text{ per m}^2 \text{ m}^{-2}$).

3.4. Emergent Constraints of Greening Effect on Ecosystem Carbon Stock

Among the 40 models, there was a strong positive correlation between the sensitivities of GPP and C stock to LAI ($R^2 = 0.63$, $P < 0.001$; Figure 4a) since the 1980s. Combining the satellite-derived sensitivities of GPP to LAI and the model-based sensitivities of C stock to LAI, we constrained the magnitude of the greening effect on C stock. The constrained greening effect on C stock ($0.75 \pm 0.46 \text{ kg C m}^{-2} \text{ per m}^2 \text{ m}^{-2}$) was lower than the model ensemble mean value ($1.63 \pm 1.29 \text{ kg C m}^{-2} \text{ per m}^2 \text{ m}^{-2}$), with a reduction of 64.54% in the range of uncertainty (Figure 4b). Additional emergent constraint analyses based on the rigorous matches of temporal duration from 1982 to 2005 in all model simulations and satellite-derived observations were performed to overcome the possible bias due to temporal variations (Winkler, Myneni, & Brovkin, 2019). The constrained results ($0.79 \pm 0.50 \text{ kg C m}^{-2} \text{ per m}^2 \text{ m}^{-2}$) by strict temporal period matching (Figure S9 in Supporting Information S1) were slightly higher than those with non-strict time-period matching ($0.75 \pm 0.46 \text{ kg C m}^{-2} \text{ per m}^2 \text{ m}^{-2}$). A further sensitivity analysis of the emerged relationship to the number of included models showed that the emerged relationship is not sensitive to the number of included models (Figure S10 in Supporting Information S1). Additionally, considering a similar result produced within the same modeling center (Todd-Brown et al., 2013, 2014), the emerged relationship which includes more models can generate a more robustness result (Figure S10 in Supporting Information S1).

The greening effect on C stock varied among the three MIPs (Figures 1d and 2e and Figure 4a). TRENDY had the highest greening sensitivity of C stock ($1.91 \pm 1.20 \text{ kg C m}^{-2} \text{ per m}^2 \text{ m}^{-2}$), followed by CMIP6 ($1.54 \pm 1.11 \text{ kg C m}^{-2} \text{ per m}^2 \text{ m}^{-2}$) and CMIP5 ($1.48 \pm 1.50 \text{ kg C m}^{-2} \text{ per m}^2 \text{ m}^{-2}$). The constrained sensitivities

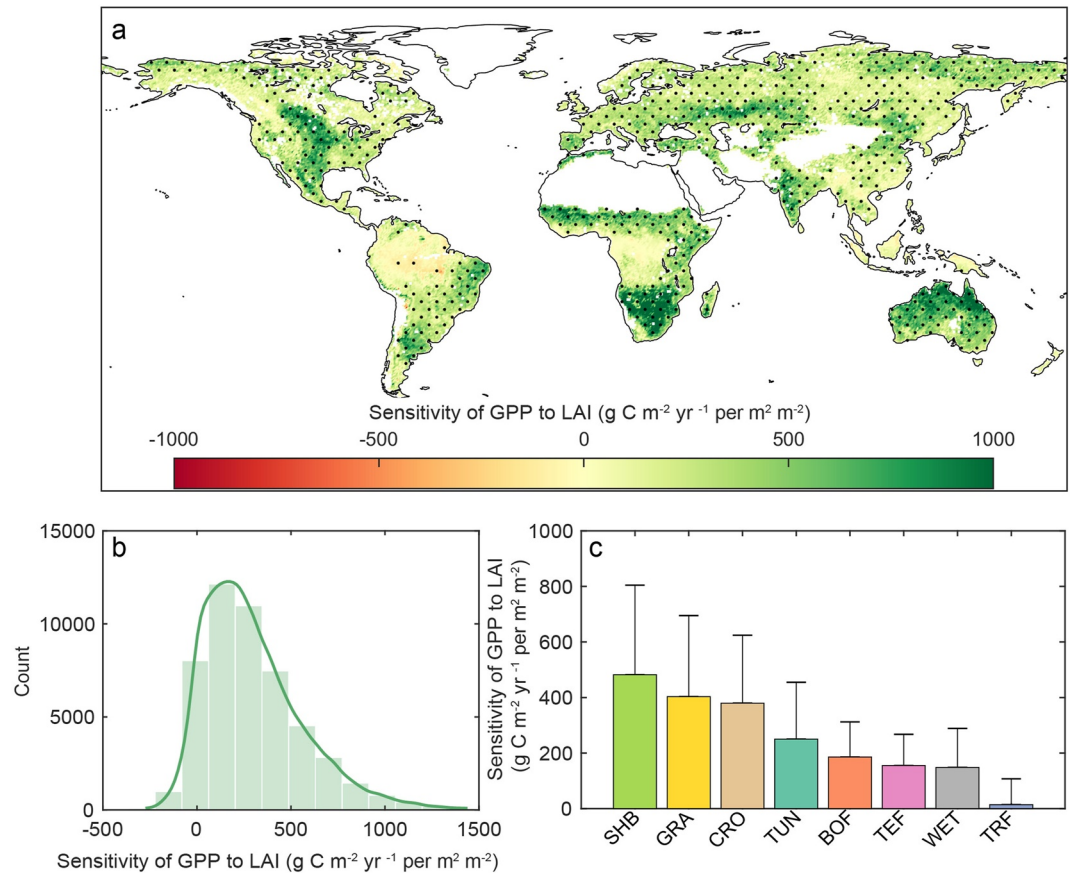


Figure 3. Positive greening effect on gross primary productivity (GPP) mainly occurred in the regions with low leaf area index (LAI). (a) Spatial pattern of the sensitivity of GPP to LAI based on the satellite observed products from 1982 to 2014. The statistically significant regions based on a *t*-test with 95% significant levels ($P < 0.05$) are represented by hatching points. (b) Histogram of GPP to LAI based on the all vegetated area grid. The distribution is represented by a green line based on the method of “kernel.” (c) Bar plot of in sensitivity of GPP to LAI in eight biomes based on MODIS land cover product (MCD12C1). The abbreviations in this panel indicate shrubland (SHB), grassland (GRA), cropland (CRO), tundra (TUN), boreal forest (BOF), temperate forest (TEF), wetland (WET), and tropical forest (TRF), respectively. The error bars in this panel indicate the standard deviation.

of C stock to LAI were 1.22 ± 0.30 , 0.28 ± 0.69 , and 0.29 ± 0.70 kg C m⁻² per m² m⁻² for TRENDY, CMIP6, and CMIP5, respectively. The uncertainty spread was reduced by 75%, 54%, and 38% for TRENDY, CMIP5, and CMIP6, respectively (Figure S11 in Supporting Information S1).

3.5. Spatial Variation of Greening Effect on Ecosystem Carbon Stock

Using the emergent constraint approach, we then constrained the greening effect on ECS on a global scale for each pixel. Compared with the multi-model ensemble means (Figure 4c), the constrained results show reduced spatial heterogeneity and a dampened greening effect on ECS, with 87.5% of global vegetated pixels showing a positive greening effect (Figure 4d). Our results showed that the constrained greening effect on ECS average over only vegetated grid cells of 0.40 ± 0.71 is 44% lower than that of the multi-model ensemble mean of 0.72 ± 0.81 kg C m⁻² per m² m⁻². Then, we classified the greening effect on ECS before and after constraint into eight biomes. As shown in Figure S12 in Supporting Information S1, the constrained greening effect on C stock decreases most in TRFs with 87.9%, followed by tundra (61.0%), TEFs (53.7%), BOF (44.0%), wetlands (33.7%), cropland (23.9%), grassland (21.6%), and shrubland (6.4%). We examined the constrained spatial pattern by applying multiple lines of data sets, such as eddy-flux observations and AGB C based on harmonized VOD data. First, we examined the relationship between annual NEP and annual mean LAI using flux-tower measurements from FLUXNET at each flux site with at least 5 years of data (Figure S13 and Table

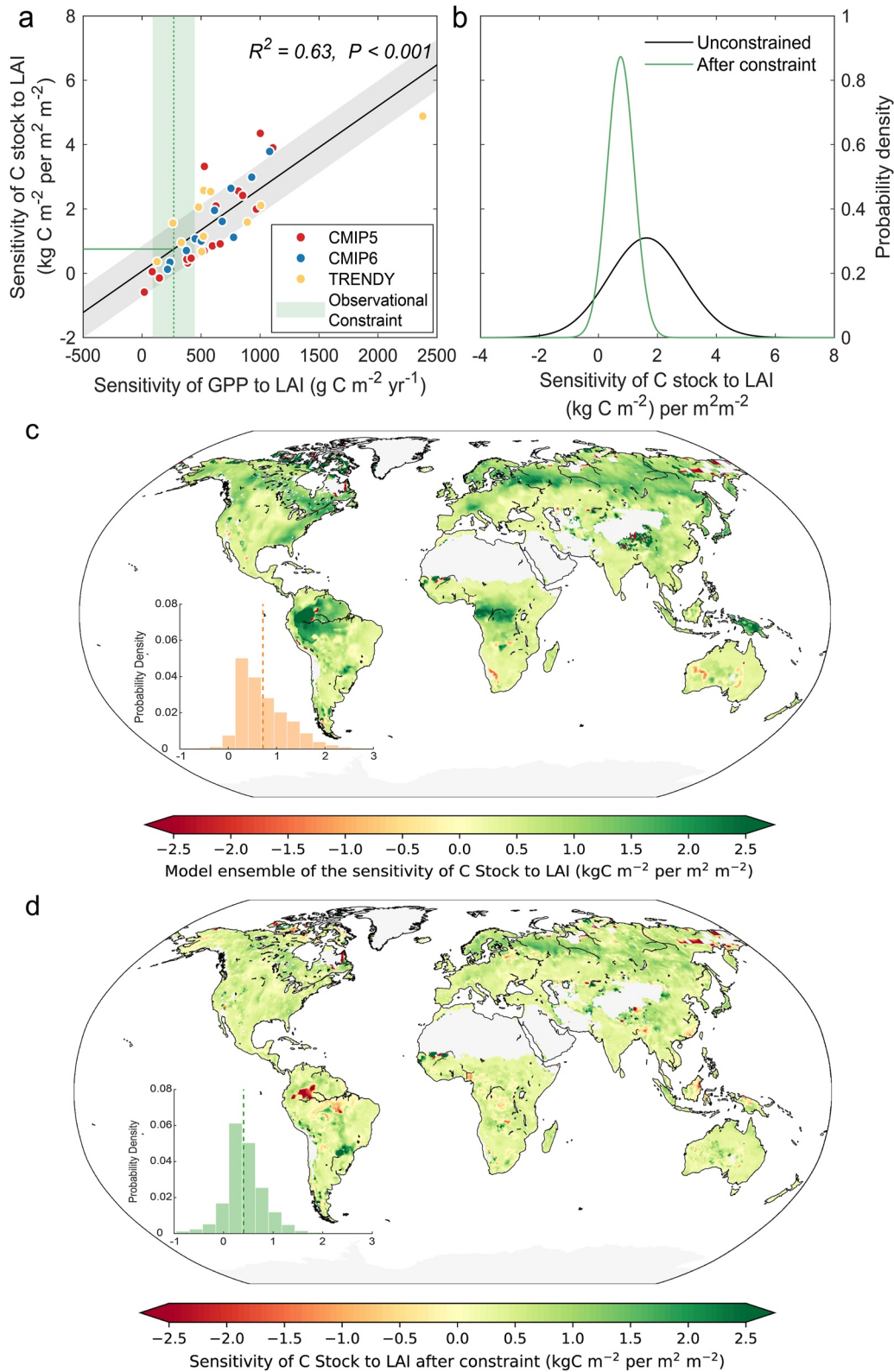


Figure 4.

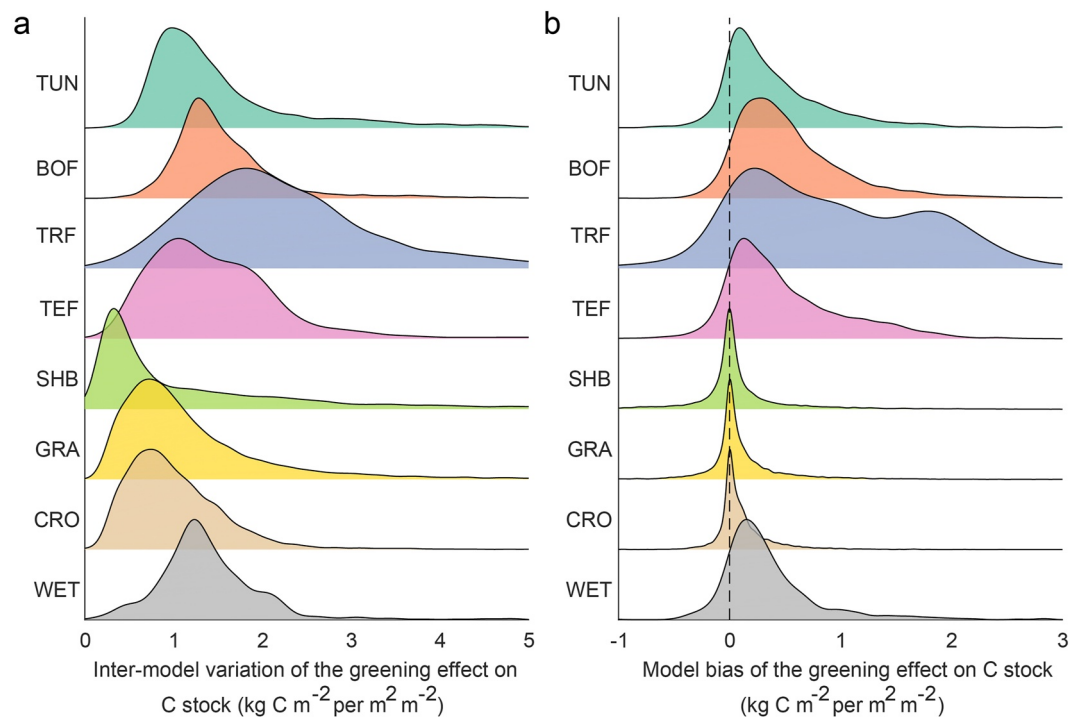


Figure 5. Ridgeline probability density plots show the comparisons of the inter-model variation (a) and model bias (b) of the greening effect on C stock among different biomes. Inter-model variation is represented by the standard deviation of the greening effect on C stock among all the 40 global models used in this study, while the model bias used here comes from the difference between multi-model ensemble results and the constrained results.

S4 in Supporting Information S1). Results show that the mean slope of all sites is $0.23 \pm 0.11 \text{ kg C m}^{-2} \text{ yr}^{-1}$, which significantly differs from zero ($P < 0.001$) (Figure S14a in Supporting Information S1). Although trends are rarely significant (13.4%) and highly variable across the sites, 63.41% of all sites showed a positive correlation between NEP and LAI (Figure S14b in Supporting Information S1). In addition, the mean values of greening effects on NEP were 0.33 ($n = 24$), 0.25 ($n = 51$), and -0.27 ($n = 7$) $\text{kg C m}^{-2} \text{ yr}^{-1}$ for the LAI ranges of <1.5 , from 1.5 to 3 , and >3 , respectively (Figure S14c in Supporting Information S1; all $P < 0.05$). Additional greening effect analyses based on the AGB C generated from VOD data show the most extensive significant positive greening effect (t -test, $P < 0.05$) in 32% of vegetated land grids (Figure S15 in Supporting Information S1). The spatial pattern of the greening effect on AGB is similar to that of GPP. The results show that shrubland had the highest sensitivity of AGB C to per unit of LAI change with $5.05 \pm 4.79 \text{ Mg C ha}^{-1} \text{ per m}^2 \text{ m}^{-2}$, but TRFs had a negative response with $-0.29 \pm 4.34 \text{ Mg C ha}^{-1} \text{ per m}^2 \text{ m}^{-2}$ (Figure S15c in Supporting Information S1).

We further compared the difference between the inter-model variation and model bias for the eight biomes (Figure 5). The results showed that the inter-model variation and the model of the greening effect on C stock have a good spatial consistency. Especially, the TRFs have the highest inter-model variation and model bias. Tundra, BOF, TEF, and wetland have mediated inter-model variation and model bias, while shrubland, grassland, and cropland have low inter-model variation and model bias (Figure 5).

Figure 4. Emergent constraint on the sensitivity of ecosystem carbon stock to leaf area index (LAI). (a) The correlation between the sensitivity of gross primary productivity (GPP) to LAI and the sensitivity of C stock to LAI. The green dash-line and shading areas indicate the mean and the range of the observational uncertainty of the sensitivity of GPP to LAI, respectively. The black straight line shows the linear regression relationship across the three MIPs ensemble together with the prediction error (gray shading areas). The green horizontal line shows the constrained sensitivity of C stock to LAI. Each scatter represents a model, red, blue, and yellow indicating Coupled Model Intercomparison Project, Coupled Model Intercomparison Project Phase 6, and TRENDY, respectively. (b) The probability distribution function for the LAI sensitivity of C stock. The black line indicates the Gaussian distribution of the original unweighted model ensemble of C stock to LAI. The green line is the satellite-derived data-constrained probability distribution of the sensitivity of C stock to LAI. Spatial distribution of the multi-model ensemble means of the sensitivity of C stock to LAI (c) and the constrained sensitivity of C stock to LAI (d). The insert panel shows the corresponding frequency distribution of the sensitivity, and the dashed line represents the mean value.

4. Discussion

This study shows a positive impact of global land greening on terrestrial ECS during the past three decades. This finding is consistent with recent empirical evidence on the associated increases in vegetation biomass (Fang et al., 2014; C. Zhu & Xia, 2020) and soil C stock (G. Zhou et al., 2006; J. Zhu et al., 2020) in terrestrial ecosystems since the 1980s. The enhanced net primary productivity with land greening can be an important mechanism underlying the increase in terrestrial ECS (Figure S16a in Supporting Information S1). Based on the satellite data, this study constrains the positive greening effect on global terrestrial ECS to $0.75 \pm 0.46 \text{ kg C m}^{-2}$ per unit LAI increase (Figure 4a). Hajima et al. (2014) used the sensitivity of GPP to LAI (GPP/LAI) as a proxy to represent leaf-level photosynthesis. Similarly, the ECS divided by LAI (ECS/LAI) could represent leaf-level carbon sequestration. These results suggest that increases in leaf area have led to a proportional increase in photosynthesis and C stock. The constrained results in Figure 4a represent leaf-level carbon sequestration, which is overestimated by most global models. Additionally, all models in the three MIPs have shown a shortening of ecosystem C residence time during the past three decades. Thus, the positive greening effect on ECS (Figure 1d) mainly results from the considerable increase in net primary productivity rather than the decrease in ecosystem C residence time (Figure S16 in Supporting Information S1).

The magnitude of the greening effect on C stock has a sizable inter-model variation, ranging from -0.59 to 4.88 kg C m^{-2} per $\text{m}^2 \text{ m}^{-2}$ (Figure 1d) among three MIPs. Compared with CMIP5 and CMIP6, the TRENDY project shows a higher constrained sensitivity of C stock to LAI with less uncertainty (Figure S11 in Supporting Information S1). The model simulations in the TRENDY project are forced by the same set of climate reanalysis data sets, which avoids the uncertainty from climate models. Most models have simulated a higher positive impact of land greening on ECS than the data-constrained result (Figure 4a). Some missing processes in current models could lead to the highly variable greening effect on C stock. First, nearly half of the models (20 out of 40) used in this study do not consider nutrient limitations (Tables S1–S3 in Supporting Information S1), especially the widespread phosphorus limitation (38 out of 40 models) throughout the global terrestrial ecosystems (Du et al., 2018; Elser et al., 2007; Wieder et al., 2015) (The simulated greening effect on C stock was 1.84 ± 1.37 for only C models, 1.42 ± 1.20 for CN models, and $1.31 \pm 0.91 \text{ kg C m}^{-2}$ per $\text{m}^2 \text{ m}^{-2}$ for CNP models; Table S6 in Supporting Information S1). Second, one critical limiting factor for land carbon uptake is soil moisture (Green et al., 2019; Humphrey et al., 2018, 2021), but many ESMs have high degrees of uncertainty in plant hydraulic processes, such as the xylem embolism (Franks et al., 2017; Konings et al., 2017) and drought legacy effect (Anderegg et al., 2015) or lack representation of such processes. Third, most ESMs used in this study did not represent the shifts in plant community structure and composition (Medlyn et al., 2015), which could weaken the positive response of ecosystem productivity and enhance the ecosystem turnover rates to increasing atmospheric CO_2 (Kolby Smith et al., 2016), nitrogen deposition (Bonan & Doney, 2018; Drewniak & Gonzalez-Meler, 2017; Wei, Xia, Wang, et al., 2022), and climate change (Richardson et al., 2018). Lastly, some global models used here did not include the processes of disturbance (e.g., deforestation and fire, Table S3 in Supporting Information S1, Figure S17 in Supporting Information S1), which reduce ECS and increase land C losses (Achat et al., 2015; Walker et al., 2019). Those models thus likely have overestimated the greening effect on ECS. An additional reason for the simulated overestimation in most models is that some satellite-derived GPP data sets do not incorporate increasing CO_2 on the LUE in C3 vegetation. Thus, we selected the GPP data sets accounting for the CO_2 fertilization effect (i.e., EC-LUE and P-model) to validate the constrained results. The constrained greening effect on C stock shows a higher value ($0.82 \pm 0.58 \text{ kg C m}^{-2}$ per $\text{m}^2 \text{ m}^{-2}$ based on EC-LUE GPP and $1.15 \pm 0.68 \text{ kg C m}^{-2}$ per $\text{m}^2 \text{ m}^{-2}$ based on P-model GPP) when considering the CO_2 effect on LUE in GPP data sets (Figure S18 in Supporting Information S1). These findings indicate that models and GPP data sets need improvements for a more accurate constrained effect of global land greening on terrestrial C stock.

The large uncertainties in the simulated greening effect on C stock almost equally stem from the sensitivities of residence time and NPP to LAI in the three MIPs (Figures 2b, 2d, 2f, and 2h). By decomposing the modeled residence time into its components, we found that the sensitivities of environmental scalars to LAI have a larger uncertainty contribution than that in baseline C residence time (78% for CMIP5, 99% for CMIP6, 76% for TRENDY, and 98% for 3MIPs). This may be due to the changes in vegetation cover altering the radiative of the land surface (Duveiller et al., 2018) and thus further influencing the energy (Alkama et al., 2022; Forzieri et al., 2017; Zeng et al., 2017) and water vapor (Yuan et al., 2019) allocation via biophysical processes. Additionally, the discrepancies in disturbance processes (such as fire and land use change) among global models are an important challenge. In addition, our results also show the sensitivity of GPP to LAI is the largest contributor to this uncertainty in more than 60% of the vegetated grids (Figure 2g). One possible reason is the difference

across canopy structures used by each model in scaling up from leaf to canopy, such as big-leaf, two-leaf, or multiple-layer (Cui et al., 2019; Li et al., 2018). Furthermore, we recognized that in the regions where other components (except for GPP) are the main contributors, such as southeastern Africa, central and southern South America, central Australia, etc., using the satellite-observed sensitivity of GPP to LAI as constrain may cause some systemic errors inevitably.

This study shows that the greening effect on ECS is highly variable across different regions or biomes. The positive and the most significant impact of vegetation greening on ECS mainly occurred in the areas with low LAI (Figure 3, Figures S14 and S15 in Supporting Information S1). This is because areas of low LAI (often also water-limited) are generally more sensitive to elevated CO₂ (Z. Zhu et al., 2016). Elevated CO₂ can decrease stomatal conductance (Field et al., 1995) and reduce water loss and leaf-scale transpiration (Ukkola et al., 2016). While in high LAI regions, especially in TRFs, further increases in LAI can negatively influence ecosystem C uptake and thus affect C stock (Figures S14c and S15 in Supporting Information S1). Such a spatial pattern indicates that the global greening effect on land C stock strongly depends on the spatial distributions of the canopy structure (e.g., LAI; Figure S7 in Supporting Information S1). Our results from satellite-derived data sets indicate a minor greening effect on GPP in tropical and high LAI regions (Figure 3). The eddy-tower measurements support such patterns in the tropics, which have shown that shaded leaves (Li et al., 2018) and respiratory C losses (Srinivasan et al., 2017) increase rapidly with increasing LAI, resulting in the reverse of the initial positive greening effects on ecosystem carbon uptake (see Figure S14, for the flux sites with LAI larger than 3 m² m⁻², carbon sinks are negatively sensitive to LAI increase). Another possible reason is that many models overestimate the response of LAI to elevated CO₂ (Kolby Smith et al., 2016), especially in the mature closed-canopy forest (Duursma et al., 2016; Norby et al., 2003). Moreover, the greening effect on AGB C shows that the positive greening effects are mainly located in shrubland regions with less model bias, but the adverse effects are in tropical areas with the largest model bias (Figure S15 in Supporting Information S1, Figure 5b). We also acknowledged that the biome classification based on MODIS land cover product might lead to some uncertainty inevitably because of the mismatch between the plant functional types used in the model and observations in some grids.

5. Conclusions

In summary, the constrained results in this study reveal a positive greening effect on ECS on a global scale since the 1980s. However, the ability of vegetation to absorb CO₂ and mitigate climate change may not be as optimistic as most models predicted. In addition, there is a high spatial heterogeneity of greening impact on ECS globally. The pervasive and positive greening effect in low-LAI ecosystems implies a land C stock shift toward high-latitude regions in the North Hemisphere under further vegetation greening. This study also reveals a great uncertainty of the positive greening effects on land carbon stock in the current generation of global models, mainly caused by the ecosystem productivity at the leaf level. This finding emphasizes the need to strengthen the simulation of vegetation canopy structure in land surface models and ESMs. Furthermore, the biome-based results reveal that the TRF regions have the highest inter-model variation and model bias. Our study identifies the uncertainty source and provides constrained estimates of the greening effect on ecosystem carbon stock. These findings underscore the importance of linking vegetation structural changes to ECS dynamics in the projections of future climate-carbon cycle feedbacks.

Data Availability Statement

The model simulations of CMIP5 and CMIP6 were obtained from the Earth System Grid Federation (ESGF) data archive (<https://esgf-node.llnl.gov/projects/esgf-llnl/>). The raw model output of TRENDY is available at the following sftp site: trendy-v9@trendy.ex.ac.uk. Access will be contacting Stephen Sitch (S.A.Sitch@exeter.ac.uk). All data used in this research are publicly available from the cited literature and the following links: The GIMMS LAI are available at https://daac.ornl.gov/VEGETATION/guides/Mean_Seasonal_LAI.html. The GLOBMAP LAI data set is available at <https://zenodo.org/record/4700264#.YyLcBnbP0b8>. The GLASS LAI data set is available at <http://www.glass.umd.edu/Download.html>. The EC-LUE GPP data are available at <https://doi.org/10.6084/m9.figshare.8942336.v3>. The GPPEnh data sets can be obtained online at https://daac.ornl.gov/cgi-bin/dsvviewer.pl?ds_id=1789. The GPP based on the P-model is available at <https://zenodo.org/record/1423484#.YyLesHbPIGq>. The FLUXNET2015 data set is available online at <https://fluxnet.org/data/fluxnet2015-dataset/>. The code and

metadata used in this study for associated analysis and producing the main figures can be accessed at <https://doi.org/10.6084/m9.figshare.21118711.v1>.

Acknowledgments

This work was financially supported by the National Key R&D Program of China (2022YFF0802104) and Shanghai Pilot Program for Basic Research (TQ20220102). We acknowledge the World Climate Research Programme's Working Group on Coupled Modeling, which is responsible for CMIP. We thank the climate modeling groups for producing and making available their model output, the Earth System Grid Federation (ESGF) for archiving the data and providing access, and the multiple funding agencies who support CMIP5, CMIP6, and ESGF. This work used eddy covariance data acquired by the FLUXNET community, particularly by the following networks: AmeriFlux, AfriFlux, AsiaFlux, CarboAfrica, CarboEuropeIP, CarboItaly, CarboMont, ChinaFlux, Fluxnet-Canada, GreenGrass, KoFlux, LBA, NECC, OzFlux, TCOS-Siberia, and USCCC. We Thank the TRENDY team for the provision of the DGVM simulations, and the researchers of the Global Carbon Project for making their data publicly available. We Thank J. Nabel, S. Zaehle for valuable suggestions on interpreting the results.

References

- Achat, D. L., Fortin, M., Landmann, G., Ringeval, B., & Augusto, L. (2015). Forest soil carbon is threatened by intensive biomass harvesting. *Scientific Reports*, 5(1), 1–10. <https://doi.org/10.1038/srep15991>
- Alkama, R., Forzieri, G., Duveiller, G., Grassi, G., Liang, S., & Cescatti, A. (2022). Vegetation-based climate mitigation in a warmer and greener World. *Nature Communications*, 13(1), 1–10. <https://doi.org/10.1038/s41467-022-28305-9>
- Anderegg, W. R., Schwalm, C., Biondi, F., Camarero, J. J., Koch, G., Litvak, M., et al. (2015). Pervasive drought legacies in forest ecosystems and their implications for carbon cycle models. *Science*, 349(6247), 528–532. <https://doi.org/10.1126/science.aab1833>
- Arora, V. K., Boer, G. J., Friedlingstein, P., Eby, M., Jones, C. D., Christian, J. R., et al. (2013). Carbon-concentration and carbon-climate feedbacks in CMIP5 Earth system models. *Journal of Climate*, 26(15), 5289–5314. <https://doi.org/10.1175/JCLI-D-12-00494.1>
- Arora, V. K., Katavouta, A., Williams, R. G., Jones, C. D., Brovkin, V., Friedlingstein, P., et al. (2020). Carbon-concentration and carbon-climate feedbacks in CMIP6 models and their comparison to CMIP5 models. *Biogeosciences*, 17(16), 4173–4222. <https://doi.org/10.5194/bg-17-4173-2020>
- Ballantyne, A., Smith, W., Anderegg, W., Kauppi, P., Sarmiento, J., Tans, P., et al. (2017). Accelerating net terrestrial carbon uptake during the warming hiatus due to reduced respiration. *Nature Climate Change*, 7(2), 148–152. <https://doi.org/10.1038/nclimate3204>
- Bonan, G. B., & Doney, S. C. (2018). Climate, ecosystems, and planetary futures: The challenge to predict life in Earth system models. *Science*, 359(6375), eaam8328. <https://doi.org/10.1126/science.aam8328>
- Bond-Lamberty, B., Bailey, V. L., Chen, M., Gough, C. M., & Vargas, R. (2018). Globally rising soil heterotrophic respiration over recent decades. *Nature*, 560(7716), 80–83. <https://doi.org/10.1038/s41586-018-0358-x>
- Brienen, R. J., Caldwell, L., Duchesne, L., Voelker, S., Barichivich, J., Baliva, M., et al. (2020). Forest carbon sink neutralized by pervasive growth-lifespan trade-offs. *Nature Communications*, 11(1), 1–10. <https://doi.org/10.1038/s41467-020-17966-z>
- Chen, J. M., Ju, W., Ciais, P., Viovy, N., Liu, R., Liu, Y., & Lu, X. (2019). Vegetation structural change since 1981 significantly enhanced the terrestrial carbon sink. *Nature Communications*, 10(1), 4259. <https://doi.org/10.1038/s41467-019-12257-8>
- Chevan, A., & Sutherland, M. (1991). Hierarchical partitioning. *The American Statistician*, 45(2), 90–96. <https://doi.org/10.2307/2684366>
- Cox, P. M., Pearson, D., Booth, B. B., Friedlingstein, P., Huntingford, C., Jones, C. D., & Luke, C. M. (2013). Sensitivity of tropical carbon to climate change constrained by carbon dioxide variability. *Nature*, 494(7437), 341–344. <https://doi.org/10.1038/nature11882>
- Cui, E., Huang, K., Arain, M. A., Fisher, J. B., Huntzinger, D. N., Ito, A., et al. (2019). Vegetation functional properties determine uncertainty of simulated ecosystem productivity: A traceability analysis in the East Asian monsoon region. *Global Biogeochemical Cycles*, 33(6), 668–689. <https://doi.org/10.1029/2018GB005909>
- Drewniak, B., & Gonzalez-Meler, M. A. (2017). Earth system model needs for including the interactive representation of nitrogen deposition and drought effects on forested ecosystems. *Forests*, 8(8), 267. <https://doi.org/10.3390/f8080267>
- Du, Z., Weng, E., Jiang, L., Luo, Y., Xia, J., & Zhou, X. (2018). Carbon-nitrogen coupling under three schemes of model representation: A traceability analysis. *Geoscientific Model Development*, 11(11), 4399–4416. <https://doi.org/10.5194/gmd-11-4399-2018>
- Duursma, R. A., Gimeno, T. E., Boer, M. M., Crous, K. Y., Tjoelker, M. G., & Ellsworth, D. S. (2016). Canopy leaf area of a mature evergreen Eucalyptus woodland does not respond to elevated atmospheric [CO₂] but tracks water availability. *Global Change Biology*, 22(4), 1666–1676. <https://doi.org/10.1111/gcb.13151>
- Duveiller, G., Hooker, J., & Cescatti, A. (2018). The mark of vegetation change on Earth's surface energy balance. *Nature Communications*, 9(1), 1–12. <https://doi.org/10.1038/s41467-017-02810-8>
- Elser, J. J., Bracken, M. E., Cleland, E. E., Gruner, D. S., Harpole, W. S., Hillebrand, H., et al. (2007). Global analysis of nitrogen and phosphorus limitation of primary producers in freshwater, marine and terrestrial ecosystems. *Ecology Letters*, 10(12), 1135–1142. <https://doi.org/10.1111/j.1461-0248.2007.01113.x>
- Eyring, V., Bony, S., Meehl, G. A., Senior, C. A., Stevens, B., Stouffer, R. J., & Taylor, K. E. (2016). Overview of the Coupled Model Inter-comparison project phase 6 (CMIP6) experimental design and organization. *Geoscientific Model Development*, 9(5), 1937–1958. <https://doi.org/10.5194/gmd-9-1937-2016>
- Eyring, V., Cox, P. M., Flato, G. M., Gleckler, P. J., Abramowitz, G., Caldwell, P., et al. (2019). Taking climate model evaluation to the next level. *Nature Climate Change*, 9(2), 102–110. <https://doi.org/10.1038/s41558-018-0355-y>
- Fang, J., Kato, T., Guo, Z., Yang, Y., Hu, H., Shen, H., et al. (2014). Evidence for environmentally enhanced forest growth. *Proceedings of the National Academy of Sciences*, 111(26), 9527–9532. <https://doi.org/10.1073/pnas.1402333111>
- Field, C. B., Jackson, R. B., & Mooney, H. A. (1995). Stomatal responses to increased CO₂: Implications from the plant to the global scale. *Plant, Cell and Environment*, 18(10), 1214–1225. <https://doi.org/10.1111/j.1365-3040.1995.tb00630.x>
- Forzieri, G., Alkama, R., Miralles, D. G., & Cescatti, A. (2017). Satellites reveal contrasting responses of regional climate to the widespread greening of Earth. *Science*, 356(6343), 1180–1184. <https://doi.org/10.1126/science.aal1727>
- Franks, P. J., Berry, J. A., Lombardozzi, D. L., & Bonan, G. B. (2017). Stomatal function across temporal and spatial scales: Deep-time trends, land-atmosphere coupling and global models. *Plant Physiology*, 174(2), 583–602. <https://doi.org/10.1104/pp.17.00287>
- Friedl, M. A., Sulla-Menashe, D., Tan, B., Schneider, A., Ramankutty, N., Sibley, A., & Huang, X. (2010). MODIS Collection 5 global land cover: Algorithm refinements and characterization of new datasets. *Remote Sensing of Environment*, 114(1), 168–182. <https://doi.org/10.1016/j.rse.2009.08.016>
- Friedlingstein, P., Meinshausen, M., Arora, V. K., Jones, C. D., Anav, A., Liddicoat, S. K., & Knutti, R. (2014). Uncertainties in CMIP5 climate projections due to carbon cycle feedbacks. *Journal of Climate*, 27(2), 511–526. <https://doi.org/10.1175/JCLI-D-12-00579.1>
- Friedlingstein, P., O'sullivan, M., Jones, M. W., Andrew, R. M., Hauck, J., Olsen, A., et al. (2020). Global carbon budget 2020. *Earth System Science Data*, 12(4), 3269–3340. <https://doi.org/10.5194/essd-12-3269-2020>
- Gelaro, R., McCarty, W., Suárez, M. J., Todling, R., Molod, A., Takacs, L., et al. (2017). The modern-era retrospective analysis for research and applications, version 2 (MERRA-2). *Journal of Climate*, 30(14), 5419–5454. <https://doi.org/10.1175/JCLI-D-16-0758.1>
- Graven, H. D., Keeling, R. F., Piper, S. C., Patra, P. K., Stephens, B. B., Wofsy, S. C., et al. (2013). Enhanced seasonal exchange of CO₂ by northern ecosystems since 1960. *Science*, 341(6150), 1085–1089. <https://doi.org/10.1126/science.1239207>
- Green, J. K., Seneviratne, S. I., Berg, A. M., Findell, K. L., Hagemann, S., Lawrence, D. M., & Gentine, P. (2019). Large influence of soil moisture on long-term terrestrial carbon uptake. *Nature*, 565(7740), 476–479. <https://doi.org/10.1038/s41586-018-0848-x>

- Hajima, T., Tachiiri, K., Ito, A., & Kawamiya, M. (2014). Uncertainty of concentration–terrestrial carbon feedback in Earth System Models. *Journal of Climate*, 27(9), 3425–3445. <https://doi.org/10.1175/JCLI-D-13-00177.1>
- Hall, A., Cox, P., Huntingford, C., & Klein, S. (2019). Progressing emergent constraints on future climate change. *Nature Climate Change*, 9(4), 269–278. <https://doi.org/10.1038/s41558-019-0436-6>
- Hastie, T., & Tibshirani, R. (1986). Generalized additive models. *Statistical Science*, 1(3), 297–310. <https://doi.org/10.1214/ss/1177013604>
- Huang, K., Xia, J., Wang, Y., Ahlström, A., Chen, J., Cook, R. B., et al. (2018). Enhanced peak growth of global vegetation and its key mechanisms. *Nature Ecology & Evolution*, 2(12), 1897–1905. <https://doi.org/10.1038/s41559-018-0714-0>
- Huang, M., Piao, S., Ciais, P., Peñuelas, J., Wang, X., Keenan, T. F., et al. (2019). Air temperature optima of vegetation productivity across global biomes. *Nature Ecology & Evolution*, 3(5), 772–779. <https://doi.org/10.1038/s41559-019-0838-x>
- Humphrey, V., Berg, A., Ciais, P., Gentine, P., Jung, M., Reichstein, M., et al. (2021). Soil moisture–atmosphere feedback dominates land carbon uptake variability. *Nature*, 592(7852), 65–69. <https://doi.org/10.1038/s41586-021-03325-5>
- Humphrey, V., Zscheischler, J., Ciais, P., Gudmundsson, L., Sitch, S., & Seneviratne, S. I. (2018). Sensitivity of atmospheric CO₂ growth rate to observed changes in terrestrial water storage. *Nature*, 560(7720), 628–631. <https://doi.org/10.1038/s41586-018-0424-4>
- Jiang, L., Shi, Z., Xia, J., Liang, J., Lu, X., Wang, Y., & Luo, Y. (2017). Transient traceability analysis of land carbon storage dynamics: Procedures and its application to two forest ecosystems. *Journal of Advances in Modeling Earth Systems*, 9(8), 2822–2835. <https://doi.org/10.1002/2017MS001004>
- Keenan, T. F., Prentice, I. C., Canadell, J. G., Williams, C. A., Wang, H., Raupach, M., & Collatz, G. J. (2016). Recent pause in the growth rate of atmospheric CO₂ due to enhanced terrestrial carbon uptake. *Nature Communications*, 7(1), 1–10. <https://doi.org/10.1038/ncomms13428>
- Kolby Smith, W., Reed, S. C., Cleveland, C. C., Ballantyne, A. P., Anderegg, W. R., Wieder, W. R., et al. (2016). Large divergence of satellite and Earth system model estimates of global terrestrial CO₂ fertilization. *Nature Climate Change*, 6(3), 306–310. <https://doi.org/10.1038/nclimate2879>
- Konings, A. G., Williams, A. P., & Gentine, P. (2017). Sensitivity of grassland productivity to aridity controlled by stomatal and xylem regulation. *Nature Geoscience*, 10(4), 284–288. <https://doi.org/10.1038/ngeo2903>
- Lawrence, D. M., Hurtt, G. C., Arneeth, A., Brovkin, V., Calvin, K. V., Jones, A. D., et al. (2016). The Land Use Model Intercomparison Project (LUMIP) contribution to CMIP6: Rationale and experimental design. *Geoscientific Model Development*, 9(9), 2973–2998. <https://doi.org/10.5194/gmd-9-2973-2016>
- Le Quéré, C., Andrew, R. M., Friedlingstein, P., Sitch, S., Hauck, J., Pongratz, J., et al. (2018). Global carbon budget 2018. *Earth System Science Data*, 10(4), 2141–2194. <https://doi.org/10.5194/essd-10-2141-2018>
- Li, Q., Lu, X., Wang, Y., Huang, X., Cox, P. M., & Luo, Y. (2018). Leaf area index identified as a major source of variability in modeled CO₂ fertilization. *Biogeosciences*, 15(22), 6909–6925. <https://doi.org/10.5194/bg-15-6909-2018>
- Lian, X., Piao, S., Huntingford, C., Li, Y., Zeng, Z., Wang, X., et al. (2018). Partitioning global land evapotranspiration using CMIP5 models constrained by observations. *Nature Climate Change*, 8(7), 640–646. <https://doi.org/10.1038/s41558-018-0207-9>
- Liu, Y., Liu, R., & Chen, J. M. (2012). Retrospective retrieval of long-term consistent global leaf area index (1981–2011) from combined AVHRR and MODIS data. *Journal of Geophysical Research*, 117(G4), 4003. <https://doi.org/10.1029/2012JG002084>
- Liu, Y. Y., Van Dijk, A. I., De Jeu, R. A., Canadell, J. G., McCabe, M. F., Evans, J. P., & Wang, G. (2015). Recent reversal in loss of global terrestrial biomass. *Nature Climate Change*, 5(5), 470–474. <https://doi.org/10.1038/nclimate2581>
- Lu, X., Wang, Y. P., Luo, Y., & Jiang, L. (2018). Ecosystem carbon transit versus turnover times in response to climate warming and rising atmospheric CO₂ concentration. *Biogeosciences*, 15(21), 6559–6572. <https://doi.org/10.5194/bg-15-6559-2018>
- Luo, Y., Ahlström, A., Allison, S. D., Batjes, N. H., Brovkin, V., Carvalhais, N., et al. (2016). Toward more realistic projections of soil carbon dynamics by Earth system models. *Global Biogeochemical Cycles*, 30(1), 40–56. <https://doi.org/10.1002/2015GB005239>
- Luo, Y., Shi, Z., Lu, X., Xia, J., Liang, J., Jiang, J., et al. (2017). Transient dynamics of terrestrial carbon storage: Mathematical foundation and its applications. *Biogeosciences*, 14(1), 145–161. <https://doi.org/10.5194/bg-14-145-2017>
- Luo, Y., White, L. W., Canadell, J. G., DeLucia, E. H., Ellsworth, D. S., Finzi, A., et al. (2003). Sustainability of terrestrial carbon sequestration: A case study in Duke Forest with inversion approach. *Global Biogeochemical Cycles*, 17(1), 1021. <https://doi.org/10.1029/2002GB001923>
- Madani, N., Kimball, J. S., & Running, S. W. (2017). Improving global gross primary productivity estimates by computing optimum light use efficiencies using flux tower data. *Journal of Geophysical Research: Biogeosciences*, 122(11), 2939–2951. <https://doi.org/10.1002/2017JG004142>
- Madani, N., Parazoo, N. C., Kimball, J. S., Ballantyne, A. P., Reichle, R. H., Maneta, M., et al. (2020). Recent amplified global gross primary productivity due to temperature increase is offset by reduced productivity due to water constraints. *AGU Advances*, 1(4), e2020AV000180. <https://doi.org/10.1029/2020AV000180>
- Mahowald, N., Lo, F., Zheng, Y., Harrison, L., Funk, C., Lombardozzi, D., & Goodale, C. (2016). Projections of leaf area index in Earth system models. *Earth System Dynamics*, 7(1), 211–229. <https://doi.org/10.5194/esd-7-211-2016>
- Mangan, S. A., Schnitzer, S. A., Herre, E. A., Mack, K. M., Valencia, M. C., Sanchez, E. I., & Bever, J. D. (2010). Negative plant–soil feedback predicts tree–species relative abundance in a tropical forest. *Nature*, 466(7307), 752–755. <https://doi.org/10.1038/nature09273>
- Mao, J., Shi, X., Thornton, P., Hoffman, F., Zhu, Z., & Myneni, R. (2013). Global latitudinal-asymmetric vegetation growth trends and their driving mechanisms: 1982–2009. *Remote Sensing*, 5(3), 1484–1497. <https://doi.org/10.3390/rs5031484>
- Medlyn, B. E., Zaehle, S., De Kauwe, M. G., Walker, A. P., Dietze, M. C., Hanson, P. J., et al. (2015). Using ecosystem experiments to improve vegetation models. *Nature Climate Change*, 5(6), 528–534. <https://doi.org/10.1038/nclimate2621>
- Meehl, G. A., Boer, G. J., Covey, C., Latif, M., & Stouffer, R. J. (2000). The coupled model intercomparison project (CMIP). *Bulletin of the American Meteorological Society*, 81(2), 313–318. [https://doi.org/10.1175/1520-0477\(2000\)081<0313:tcmpic>2.3.co;2](https://doi.org/10.1175/1520-0477(2000)081<0313:tcmpic>2.3.co;2)
- Meehl, G. A., Covey, C., McAvaney, B., Latif, M., & Stouffer, R. J. (2005). Overview of the coupled model intercomparison project. *Bulletin of the American Meteorological Society*, 86(1), 89–93. Retrieved from <http://www.jstor.org/stable/26221235>
- Meehl, G. A., Moss, R., Taylor, K. E., Eyring, V., Stouffer, R. J., Bony, S., & Stevens, B. (2014). Climate model intercomparisons: Preparing for the next phase. *Eos, Transactions American Geophysical Union*, 95(9), 77–78. <https://doi.org/10.1002/2014EO090001>
- Murray, K., & Conner, M. M. (2009). Methods to quantify variable importance: Implications for the analysis of noisy ecological data. *Ecology*, 90(2), 348–355. <https://doi.org/10.1890/07-1929.1>
- Myneni, R. B., Keeling, C. D., Tucker, C. J., Asrar, G., & Nemani, R. R. (1997). Increased plant growth in the northern high latitudes from 1981 to 1991. *Nature*, 386(6626), 698–702. <https://doi.org/10.1038/386698a0>
- Norby, R. J., Sholtis, J. D., Gunderson, C. A., & Jawdy, S. S. (2003). Leaf dynamics of a deciduous forest canopy: No response to elevated CO₂. *Oecologia*, 136(4), 574–584. <https://doi.org/10.1007/s00442-003-1296-2>
- O'Sullivan, M., Smith, W. K., Sitch, S., Friedlingstein, P., Arora, V. K., Haverd, V., et al. (2020). Climate-driven variability and trends in plant productivity over recent decades based on three global products. *Global Biogeochemical Cycles*, 34(12), e2020GB006613. <https://doi.org/10.1029/2020GB006613>

- Pan, Y., Birdsey, R. A., Fang, J., Houghton, R., Kauppi, P. E., Kurz, W. A., et al. (2011). A large and persistent carbon sink in the world's forests. *Science*, 333(6045), 988–993. <https://doi.org/10.1126/science.1201609>
- Papale, D., Reichstein, M., Aubinet, M., Canfora, E., Bernhofer, C., Kutsch, W., et al. (2006). Towards a standardized processing of net ecosystem exchange measured with eddy covariance technique: Algorithms and uncertainty estimation. *Biogeosciences*, 3(4), 571–583. <https://doi.org/10.5194/bg-3-571-2006>
- Piao, S., Liu, Q., Chen, A., Janssens, I. A., Fu, Y., Dai, J., et al. (2019). Plant phenology and global climate change: Current progresses and challenges. *Global Change Biology*, 25(6), 1922–1940. <https://doi.org/10.1111/gcb.14619>
- Piao, S., Wang, X., Park, T., Chen, C., Lian, X. U., He, Y., et al. (2020). Characteristics, drivers and feedbacks of global greening. *Nature Reviews Earth & Environment*, 1(1), 14–27. <https://doi.org/10.1038/s43017-019-0001-x>
- Prentice, I. C., Liang, X., Medlyn, B. E., & Wang, Y. P. (2015). Reliable, robust and realistic: The three R's of next-generation land-surface modelling. *Atmospheric Chemistry and Physics*, 15(10), 5987–6005. <https://doi.org/10.5194/acp-15-5987-2015>
- Qian, H., Joseph, R., & Zeng, N. (2010). Enhanced terrestrial carbon uptake in the Northern High Latitudes in the 21st century from the Coupled Carbon Cycle Climate Model Intercomparison Project model projections. *Global Change Biology*, 16(2), 641–656. <https://doi.org/10.1111/j.1365-2486.2009.01989.x>
- Richardson, A. D., Hufkens, K., Milliman, T., Aubrecht, D. M., Furze, M. E., Seyednasrollah, B., et al. (2018). Ecosystem warming extends vegetation activity but heightens vulnerability to cold temperatures. *Nature*, 560(7718), 368–371. <https://doi.org/10.1038/s41586-018-0399-1>
- Running, S. W., Nemani, R. R., Heinsch, F. A., Zhao, M., Reeves, M., & Hashimoto, H. (2004). A continuous satellite-derived measure of global terrestrial primary production. *BioScience*, 54(6), 547–560. [https://doi.org/10.1641/0006-3568\(2004\)054\[0547:ACSMOG\]2.0.CO;2](https://doi.org/10.1641/0006-3568(2004)054[0547:ACSMOG]2.0.CO;2)
- Saatchi, S. S., Morel, A., Brown, S., Lefsky, M., Mitchard, E. T. A., Salas, W., et al. (2011). Benchmark map of forest carbon stocks in tropical regions across three continents. *Proceedings of the National Academy of Sciences of the United States of America*, 108(24), 9899–9904. <https://doi.org/10.1073/pnas.1019576108>
- Srinivasan, V., Kumar, P., & Long, S. P. (2017). Decreasing, not increasing, leaf area will raise crop yields under global atmospheric change. *Global Change Biology*, 23(4), 1626–1635. <https://doi.org/10.1111/gcb.13526>
- Stocker, B. (2018). sofun: V1.1.0. *Zenodo*. <https://doi.org/10.5281/zenodo.1213758>
- Stocker, B. D., Zscheischler, J., Keenan, T. F., Prentice, I. C., Peñuelas, J., & Seneviratne, S. I. (2018). Quantifying soil moisture impacts on light use efficiency across biomes. *New Phytologist*, 218(4), 1430–1449. <https://doi.org/10.1111/nph.15123>
- Stocker, B. D., Zscheischler, J., Keenan, T. F., Prentice, I. C., Seneviratne, S. I., & Peñuelas, J. (2019). Drought impacts on terrestrial primary production underestimated by satellite monitoring. *Nature Geoscience*, 12(4), 264–270. <https://doi.org/10.1038/s41561-019-0318-6>
- Taylor, K. E., Stouffer, R. J., & Meehl, G. A. (2012). An overview of CMIP5 and the experiment design. *Bulletin of the American Meteorological Society*, 93(4), 485–498. <https://doi.org/10.1175/BAMS-D-11-00094.1>
- Todd-Brown, K. E. O., Randerson, J. T., Hopkins, F., Arora, V., Hajima, T., Jones, C., et al. (2014). Changes in soil organic carbon storage predicted by Earth system models during the 21st century. *Biogeosciences*, 11(8), 2341–2356. <https://doi.org/10.5194/bg-11-2341-2014>
- Todd-Brown, K. E. O., Randerson, J. T., Post, W. M., Hoffman, F. M., Tarnocai, C., Schuur, E. A. G., & Allison, S. D. (2013). Causes of variation in soil carbon simulations from CMIP5 Earth system models and comparison with observations. *Biogeosciences*, 10(3), 1717–1736. <https://doi.org/10.5194/bg-10-1717-2013>
- Ukkola, A. M., Keenan, T. F., Kelley, D. I., & Prentice, D. I. (2016). Vegetation plays an important role in mediating future water resources. *Environmental Research Letters*, 11(9), 094022. <https://doi.org/10.1088/1748-9326/11/9/094022>
- Van Groenigen, K. J., Qi, X., Osenberg, C. W., Luo, Y., & Hungate, B. A. (2014). Faster decomposition under increased atmospheric CO₂ limits soil carbon storage. *Science*, 344(6183), 508–509. <https://doi.org/10.1126/science.1249534>
- Varney, R. M., Chadburn, S. E., Friedlingstein, P., Burke, E. J., Koven, C. D., Hugelius, G., & Cox, P. M. (2020). A spatial emergent constraint on the sensitivity of soil carbon turnover to global warming. *Nature Communications*, 11(1), 1–8. <https://doi.org/10.1038/s41467-020-19208-8>
- Walker, X. J., Baltzer, J. L., Cumming, S. G., Day, N. J., Ebert, C., Goetz, S., et al. (2019). Increasing wildfires threaten historic carbon sink of boreal forest soils. *Nature*, 572(7770), 520–523. <https://doi.org/10.1038/s41586-019-1474-y>
- Wang, H., Prentice, I. C., Keenan, T. F., Davis, T. W., Wright, I. J., Cornwell, W. K., et al. (2017). Towards a universal model for carbon dioxide uptake by plants. *Nature Plants*, 3(9), 734–741. <https://doi.org/10.1038/s41477-017-0006-8>
- Wang, J., Xia, J., Zhou, X., Huang, K., Zhou, J., Huang, Y., et al. (2019). Evaluating the simulated mean soil carbon transit times by Earth system models using observations. *Biogeosciences*, 16(4), 917–926. <https://doi.org/10.5194/bg-16-917-2019>
- Wei, N., Xia, J., Wang, Y.-P., Zhang, X., Zhou, J., Bian, C., & Luo, Y. (2022). Nutrient limitations lead to a reduced magnitude of disequilibrium in the global terrestrial carbon cycle. *Journal of Geophysical Research: Biogeosciences*, 127(5), e2021JG006764. <https://doi.org/10.1029/2021JG006764>
- Wei, N., Xia, J., Zhou, J., Jiang, L., Cui, E., Ping, J., & Luo, Y. (2022). Evolution of uncertainty in terrestrial Carbon storage in Earth system Models from CMIP5 to CMIP6. *Journal of Climate*, 35(17), 5483–5499. <https://doi.org/10.1175/JCLI-D-21-0763.1>
- Wenzel, S., Cox, P. M., Eyring, V., & Friedlingstein, P. (2016). Projected land photosynthesis constrained by changes in the seasonal cycle of atmospheric CO₂. *Nature*, 538(7626), 499–501. <https://doi.org/10.1038/nature19772>
- Wieder, W. R., Cleveland, C. C., Smith, W. K., & Todd-Brown, K. (2015). Future productivity and carbon storage limited by terrestrial nutrient availability. *Nature Geoscience*, 8(6), 441–444. <https://doi.org/10.1038/ngeo2413>
- Winkler, A. J., Myneni, R. B., Alexandrov, G. A., & Brovkin, V. (2019). Earth system models underestimate carbon fixation by plants in the high latitudes. *Nature Communications*, 10(1), 1–8. <https://doi.org/10.1038/s41467-019-08633-z>
- Winkler, A. J., Myneni, R. B., & Brovkin, V. (2019). Investigating the applicability of emergent constraints. *Earth System Dynamics*, 10(3), 501–523. <https://doi.org/10.5194/esd-10-501-2019>
- Wu, D., Piao, S., Zhu, D., Wang, X., Ciais, P., Bastos, A., et al. (2020). Accelerated terrestrial ecosystem carbon turnover and its drivers. *Global Change Biology*, 26(9), 5052–5062. <https://doi.org/10.1111/gcb.15224>
- Xia, J., Luo, Y., Wang, Y. P., & Hararuk, O. (2013). Traceable components of terrestrial carbon storage capacity in biogeochemical models. *Global Change Biology*, 19(7), 2104–2116. <https://doi.org/10.1111/gcb.12172>
- Xia, J., McGuire, A. D., Lawrence, D., Burke, E., Chen, G., Chen, X., et al. (2017). Terrestrial ecosystem model performance in simulating productivity and its vulnerability to climate change in the northern permafrost region. *Journal of Geophysical Research: Biogeosciences*, 122(2), 430–446. <https://doi.org/10.1002/2016JG003384>
- Xiao, Z., Liang, S., Wang, J., Chen, P., Yin, X., Zhang, L., & Song, J. (2013). Use of general regression neural networks for generating the GLASS leaf area index product from time-series MODIS surface reflectance. *IEEE Transactions on Geoscience and Remote Sensing*, 52(1), 209–223. <https://doi.org/10.1109/TGRS.2013.2237780>

- Xiao, Z., Liang, S., Wang, J., Xiang, Y., Zhao, X., & Song, J. (2016). Long-time-series global land surface satellite leaf area index product derived from MODIS and AVHRR surface reflectance. *IEEE Transactions on Geoscience and Remote Sensing*, *54*(9), 5301–5318. <https://doi.org/10.1109/TGRS.2016.2560522>
- Yu, K., Smith, W. K., Trugman, A. T., Condit, R., Hubbell, S. P., Sardans, J., et al. (2019). Pervasive decreases in living vegetation carbon turnover time across forest climate zones. *Proceedings of the National Academy of Sciences*, *116*(49), 24662–24667. <https://doi.org/10.1073/pnas.1821387116>
- Yuan, W., Liu, S., Yu, G., Bonnefond, J. M., Chen, J., Davis, K., et al. (2010). Global estimates of evapotranspiration and gross primary production based on MODIS and global meteorology data. *Remote Sensing of Environment*, *114*(7), 1416–1431. <https://doi.org/10.1016/j.rse.2010.01.022>
- Yuan, W., Liu, S., Zhou, G., Zhou, G., Tieszen, L. L., Baldocchi, D., et al. (2007). Deriving a light use efficiency model from eddy covariance flux data for predicting daily gross primary production across biomes. *Agricultural and Forest Meteorology*, *143*(3–4), 189–207. <https://doi.org/10.1016/j.agrformet.2006.12.001>
- Yuan, W., Zheng, Y., Piao, S., Ciais, P., Lombardozzi, D., Wang, Y., et al. (2019). Increased atmospheric vapor pressure deficit reduces global vegetation growth. *Science Advances*, *5*(8), eaax1396. <https://doi.org/10.1126/sciadv.aax1396>
- Zeng, Z., Piao, S., Li, L. Z., Zhou, L., Ciais, P., Wang, T., et al. (2017). Climate mitigation from vegetation biophysical feedbacks during the past three decades. *Nature Climate Change*, *7*(6), 432–436. <https://doi.org/10.1038/nclimate3299>
- Zeng, Z., Zhu, Z., Lian, X., Li, L. Z., Chen, A., He, X., & Piao, S. (2016). Responses of land evapotranspiration to Earth's greening in CMIP5 Earth System Models. *Environmental Research Letters*, *11*(10), 104006. <https://doi.org/10.1088/1748-9326/11/10/104006>
- Zhang, X., Wang, Y. P., Peng, S., Rayner, P. J., Ciais, P., Silver, J. D., et al. (2018). Dominant regions and drivers of the variability of the global land carbon sink across timescales. *Global Change Biology*, *24*(9), 3954–3968. <https://doi.org/10.1111/gcb.14275>
- Zheng, Y., Shen, R., Wang, Y., Li, X., Liu, S., Liang, S., et al. (2020). Improved estimate of global gross primary production for reproducing its long-term variation, 1982–2017. *Earth System Science Data*, *12*(4), 2725–2746. <https://doi.org/10.5194/essd-12-2725-2020>
- Zhou, G., Liu, S., Li, Z., Zhang, D., Tang, X., Zhou, C., et al. (2006). Old-growth forests can accumulate carbon in soils. *Science*, *314*(5804), 1417. <https://doi.org/10.1126/science.1130168>
- Zhou, J., Xia, J., Wei, N., Liu, Y., Bian, C., Bai, Y., & Luo, Y. (2021). A traceability analysis system for model evaluation on land carbon dynamics: Design and applications. *Ecological Processes*, *10*(1), 1–14. <https://doi.org/10.1186/s13717-021-00281-w>
- Zhou, S., Liang, J., Lu, X., Li, Q., Jiang, L., Zhang, Y., et al. (2018). Sources of uncertainty in modeled land carbon storage within and across three MIPs: Diagnosis with three new techniques. *Journal of Climate*, *31*(7), 2833–2851. <https://doi.org/10.1175/JCLI-D-17-0357.1>
- Zhu, C., & Xia, J. (2020). Nonlinear increase of vegetation carbon storage in aging forests and its implications for Earth system models. *Journal of Advances in Modeling Earth Systems*, *12*(12), e2020MS002304. <https://doi.org/10.1029/2020MS002304>
- Zhu, J., Wang, C., Zhou, Z., Zhou, G., Hu, X., Jiang, L., et al. (2020). Increasing soil carbon stocks in eight permanent forest plots in China. *Biogeosciences*, *17*(3), 715–726. <https://doi.org/10.5194/bg-17-715-2020>
- Zhu, Z., Bi, J., Pan, Y., Ganguly, S., Anav, A., Xu, L., et al. (2013). Global data sets of vegetation leaf area index (LAI) 3g and fraction of photosynthetically active radiation (FPAR) 3g derived from global inventory modeling and mapping studies (GIMMS) normalized difference vegetation index (NDVI3g) for the period 1981 to 2011. *Remote Sensing*, *5*(2), 927–948. <https://doi.org/10.3390/rs5020927>
- Zhu, Z., Piao, S., Lian, X., Myneni, R. B., Peng, S., & Yang, H. (2017). Attribution of seasonal leaf area index trends in the northern latitudes with “optimally” integrated ecosystem models. *Global Change Biology*, *23*(11), 4798–4813. <https://doi.org/10.1111/gcb.13723>
- Zhu, Z., Piao, S., Myneni, R. B., Huang, M., Zeng, Z., Canadell, J. G., et al. (2016). Greening of the Earth and its drivers. *Nature Climate Change*, *6*(8), 791–795. <https://doi.org/10.1038/nclimate3004>

References From the Supporting Information

- Adachi, Y., Yukimoto, S., Deushi, M., Obata, A., Nakano, H., Tanaka, T. Y., et al. (2013). Basic performance of a new Earth system model of the Meteorological Research Institute (MRI-ESM1). *Papers in Meteorology and Geophysics*, *64*(0), 1–19. <https://doi.org/10.2467/mripapers.64.1>
- Arora, V. K., & Boer, G. J. (2010). Uncertainties in the 20th century carbon budget associated with land use change. *Global Change Biology*, *16*(12), 3327–3348. <https://doi.org/10.1111/j.1365-2486.2010.02202.x>
- Bentsen, M., Bethke, I., Debernard, J. B., Iversen, T., Kirkevåg, A., Selund, Ø., et al. (2013). The Norwegian Earth system Model, NorESM1-M—Part I: Description and basic evaluation of the physical climate. *Geoscientific Model Development*, *6*(3), 687–720. <https://doi.org/10.5194/gmd-6-687-2013>
- Boucher, O., Servonnat, J., Albright, A. L., Aumont, O., Balkanski, Y., Bastrikov, V., et al. (2020). Presentation and evaluation of the IPSL-CM6A-LR climate model. *Journal of Advances in Modeling Earth Systems*, *12*(7), e2019MS002010. <https://doi.org/10.1029/2019MS002010>
- Cherchi, A., Fogli, P. G., Lovato, T., Peano, D., Iovino, D., Gualdi, S., et al. (2019). Global mean climate and main patterns of variability in the CMCC-CM2 coupled model. *Journal of Advances in Modeling Earth Systems*, *11*(1), 185–209. <https://doi.org/10.1029/2018MS001369>
- Collins, W. J., Bellouin, N., Doutriaux-Boucher, M., Gedney, N., Halloran, P., Hinton, T., et al. (2011). Development and evaluation of an Earth-System model-HadGEM2. *Geoscientific Model Development*, *4*(4), 1051–1075. <https://doi.org/10.5194/gmd-4-1051-2011>
- Dufresne, J. L., Foujols, M. A., Denvil, S., Caubel, A., Marti, O., Aumont, O., et al. (2013). Climate change projections using the IPSL-CM5 Earth system Model: From CMIP3 to CMIP5. *Climate Dynamics*, *40*(9), 2123–2165. <https://doi.org/10.1007/s00382-012-1636-1>
- Dunne, J. P., John, J. G., Shevliakova, E., Stouffer, R. J., Krasting, J. P., Malyshev, S. L., et al. (2013). GFDL's ESM2 global coupled climate-carbon Earth system models. Part II: Carbon system formulation and baseline simulation characteristics. *Journal of Climate*, *26*(7), 2247–2267. <https://doi.org/10.1175/JCLI-D-12-00150.1>
- Gottelman, A., Hannay, C., Bacmeister, J. T., Neale, R. B., Pendergrass, A. G., Danabasoglu, G., et al. (2019). High climate sensitivity in the Community Earth system Model version 2 (CESM2). *Geophysical Research Letters*, *46*(14), 8329–8337. <https://doi.org/10.1029/2019GL083978>
- Giorgetta, M. A., Jungclaus, J., Reick, C. H., Legutke, S., Bader, J., Böttinger, M., et al. (2013). Climate and carbon cycle changes from 1850 to 2100 in MPI-ESM simulations for the Coupled Model Intercomparison Project phase 5. *Journal of Advances in Modeling Earth Systems*, *5*(3), 572–597. <https://doi.org/10.1002/jame.20038>
- Goll, D. S., Vuichard, N., Maignan, F., Jornet-Puig, A., Sardans, J., Violette, A., et al. (2017). A representation of the phosphorus cycle for ORCHIDEE (revision 4520). *Geoscientific Model Development*, *10*(10), 3745–3770. <https://doi.org/10.5194/gmd-10-3745-2017>
- Haverd, V., Smith, B., Nieradzic, L., Briggs, P. R., Woodgate, W., Trudinger, C. M., et al. (2018). A new version of the CABLE land surface model (Subversion revision r4601) incorporating land use and land cover change, woody vegetation demography, and a novel optimisation-based approach to plant coordination of photosynthesis. *Geoscientific Model Development*, *11*(7), 2995–3026. <https://doi.org/10.5194/gmd-11-2995-2018>

- Jones, C., Hughes, J. K., Bellouin, N., Hardiman, S. C., Jones, G. S., Knight, J., et al. (2011). The HadGEM2-ES implementation of CMIP5 centennial simulations. *Geoscientific Model Development*, 4(3), 543–570. <https://doi.org/10.5194/gmd-4-543-2011>
- Kato, E., Kinoshita, T., Ito, A., Kawamiya, M., & Yamagata, Y. (2013). Evaluation of spatially explicit emission scenario of land-use change and biomass burning using a process-based biogeochemical model. *Journal of Land Use Science*, 8(1), 104–122. <https://doi.org/10.1080/1747423X.2011.628705>
- Lawrence, D. M., Fisher, R. A., Koven, C. D., Oleson, K. W., Swenson, S. C., Bonan, G., et al. (2019). The Community Land Model version 5: Description of new features, benchmarking, and impact of forcing uncertainty. *Journal of Advances in Modeling Earth Systems*, 11(12), 4245–4287. <https://doi.org/10.1029/2018MS001583>
- Lee, W. L., Wang, Y. C., Shiu, C. J., Tsai, I. C., Tu, C. Y., Lan, Y. Y., et al. (2020). Taiwan Earth system Model version 1: Description and evaluation of mean state. *Geoscientific Model Development*, 13(9), 3887–3904. <https://doi.org/10.5194/gmd-13-3887-2020>
- Lienert, S., & Joos, F. (2018). A Bayesian ensemble data assimilation to constrain model parameters and land-use carbon emissions. *Biogeosciences*, 15(9), 2909–2930. <https://doi.org/10.5194/bg-15-2909-2018>
- Liu, H. L., Foster, B. T., Hagan, M. E., McNerney, J. M., Maute, A., Qian, L., et al. (2010). Thermosphere extension of the whole atmosphere community climate model. *Journal of Geophysical Research*, 115(A12), A12302. <https://doi.org/10.1029/2010JA015586>
- Mauritsen, T., Bader, J., Becker, T., Behrens, J., Bittner, M., Brokopf, R., et al. (2019). Developments in the MPI-M Earth System Model version 1.2 (MPI-ESM1.2) and its response to increasing CO₂. *Journal of Advances in Modeling Earth Systems*, 11(4), 998–1038. <https://doi.org/10.1029/2018MS001400>
- Melton, J. R., Arora, V. K., Wisernig-Cojoc, E., Seiler, C., Fortier, M., Chan, E., & Teckentrup, L. (2020). CLASSIC v1.0: The open-source community successor to the Canadian land surface Scheme (CLASS) and the Canadian terrestrial ecosystem Model (CTEM)—Part 1: Model framework and site-level performance. *Geoscientific Model Development*, 13(6), 2825–2850. <https://doi.org/10.5194/gmd-13-2825-2020>
- Reick, C. H., Gayler, V., Goll, D., Hagemann, S., Heidkamp, M., Nabel, J. E., et al. (2021). JSBACH 3—the land component of the MPI Earth system Model: Documentation of version 3.2. <https://doi.org/10.17617/2.3279802>
- Seland, Ø., Bentsen, M., Olivie, D., Toniazzo, T., Gjermundsen, A., Graff, L. S., et al. (2020). Overview of the Norwegian Earth System Model (NorESM2) and key climate response of CMIP6 DECK, historical, and scenario simulations. *Geoscientific Model Development*, 13(12), 6165–6200. <https://doi.org/10.5194/gmd-13-6165-2020>
- Sellar, A. A., Jones, C. G., Mulcahy, J. P., Tang, Y., Yool, A., Wiltshire, A., et al. (2019). UKESM1: Description and evaluation of the UK Earth system Model. *Journal of Advances in Modeling Earth Systems*, 11(12), 4513–4558. <https://doi.org/10.1029/2019MS001739>
- Swart, N. C., Cole, J. N., Kharin, V. V., Lazare, M., Scinocca, J. F., Gillett, N. P., et al. (2019). The Canadian Earth system model version 5 (CanESM5.0.3). *Geoscientific Model Development*, 12(11), 4823–4873. <https://doi.org/10.5194/gmd-12-4823-2019>
- Tjiputra, J. F., Roelandt, C., Bentsen, M., Lawrence, D. M., Lorentzen, T., Schwinger, J., et al. (2013). Evaluation of the carbon cycle components in the Norwegian Earth system Model (NorESM). *Geoscientific Model Development*, 6(2), 301–325. <https://doi.org/10.5194/gmd-6-301-2013>
- Vuichard, N., Messina, P., Luyssaert, S., Guenet, B., Zaehle, S., Ghattas, J., et al. (2019). Accounting for carbon and nitrogen interactions in the global terrestrial ecosystem model ORCHIDEE (trunk version, rev 4999): Multi-scale evaluation of gross primary production. *Geoscientific Model Development*, 12(11), 4751–4779. <https://doi.org/10.5194/gmd-12-4751-2019>
- Walker, A. P., Quaife, T., Van Bodegom, P. M., De Kauwe, M. G., Keenan, T. F., Joiner, J., et al. (2017). The impact of alternative trait-scaling hypotheses for the maximum photosynthetic carboxylation rate (V_{cmax}) on global gross primary production. *New Phytologist*, 215(4), 1370–1386. <https://doi.org/10.1111/nph.14623>
- Watanabe, S., Hajima, T., Sudo, K., Nagashima, T., Takemura, T., Okajima, H., et al. (2011). MIROC-ESM 2010: Model description and basic results of CMIP5-20c3m experiments. *Geoscientific Model Development*, 4(4), 845–872. <https://doi.org/10.5194/gmd-4-845-2011>
- Wu, T., Li, W., Ji, J., Xin, X., Li, L., Wang, Z., et al. (2013). Global carbon budgets simulated by the Beijing Climate Center Climate system Model for the last century. *Journal of Geophysical Research: Atmospheres*, 118(10), 4326–4347. <https://doi.org/10.1002/jgrd.50320>
- Wu, T., Lu, Y., Fang, Y., Xin, X., Li, L., Li, W., et al. (2019). The Beijing Climate Center climate system model (BCC-CSM): The main progress from CMIP5 to CMIP6. *Geoscientific Model Development*, 12(4), 1573–1600. <https://doi.org/10.5194/gmd-12-1573-2019>
- Wyser, K., van Noije, T., Yang, S., von Hardenberg, J., O'Donnell, D., & Döschner, R. (2020). On the increased climate sensitivity in the EC-Earth model from CMIP5 to CMIP6. *Geoscientific Model Development*, 13(8), 3465–3474. <https://doi.org/10.5194/gmd-13-3465-2020>
- Yuan, W., Liu, D., Dong, W., Liu, S., Zhou, G., Yu, G., et al. (2014). Multiyear precipitation reduction strongly decreases carbon uptake over northern China. *Journal of Geophysical Research: Biogeosciences*, 119(5), 881–896. <https://doi.org/10.1002/2014JG002608>
- Zaehle, S., & Friend, A. D. (2010). Carbon and nitrogen cycle dynamics in the O-CN land surface model: 1. Model description, site-scale evaluation, and sensitivity to parameter estimates. *Global Biogeochemical Cycles*, 24(1), 1–13. <https://doi.org/10.1029/2009GB003521>
- Ziehn, T., Chamberlain, M. A., Law, R. M., Lenton, A., Bodman, R. W., Dix, M., et al. (2020). The Australian Earth system model: ACCESS-ESM1.5. *Journal of Southern Hemisphere Earth Systems Science*, 70(1), 193–214. <https://doi.org/10.1017/ES19035>